SUPPORTING INFORMATION

Visualizing Compartmentalized Cellular Mg^{2+} on Demand with Small-Molecule Fluorescent Sensors

*Jessica J. Gruskos, Guangqian Zhang, and Daniela Buccella**

Department of Chemistry, New York University, New York, New York 10003

Table of Contents

S1. Supplemental figures

S1.1 Metal-binding properties of BCN-activated Mag-*S*-Tz

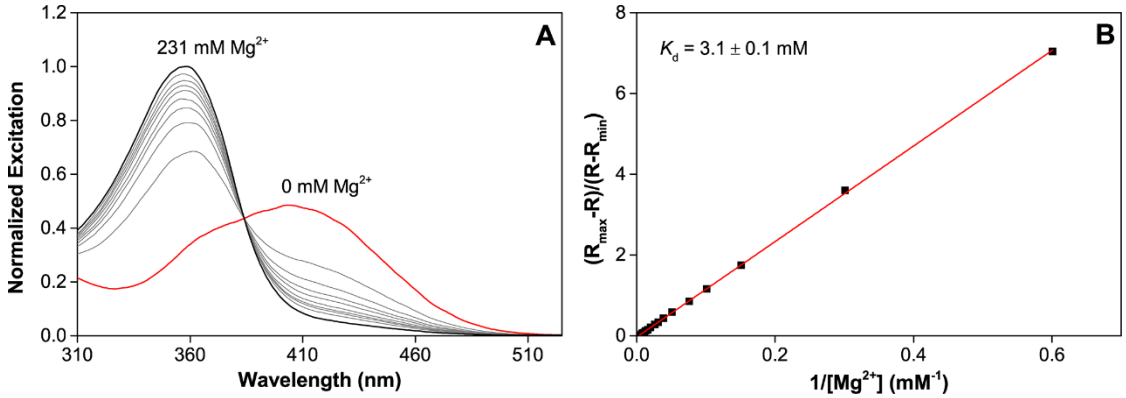

Figure S1. (A) Representative fluorescence excitation spectra of a 1 μM solution of BCN-activated sensor in aqueous buffer at pH 7.0, 25 °C, as a function of Mg^{2+} concentration. Emission wavelength: 595 nm. (B) Representative double reciprocal plot for the change in fluorescence ratio as a function of magnesium concentration. Excitation wavelengths: λ_1 = 358 nm, λ_2 = 404 nm. Dissociation constant corresponds to the average of three independent titrations.

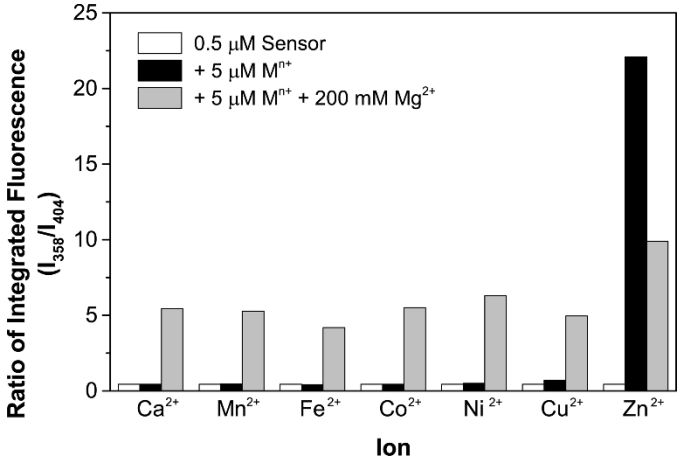

Figure S2. Metal selectivity plot for BCN-clicked sensor in aqueous buffer at pH 7.0. Data represent the fluorescence ratio of 0.5 μM sensor solution before (white bar) and after treatment with either $CaCl_2$, $MnCl_2$, $Fe(NH_4)_2(SO_4)_2$, $CoCl_2$, $NiCl_2$, $CuCl_2$, or $ZnCl_2$ in aqueous buffer for a final concentration of 5 μM M^{n+} (black bar) or 5 μM M^{n+} and 200 mM $MgCl_2$ (gray bar).

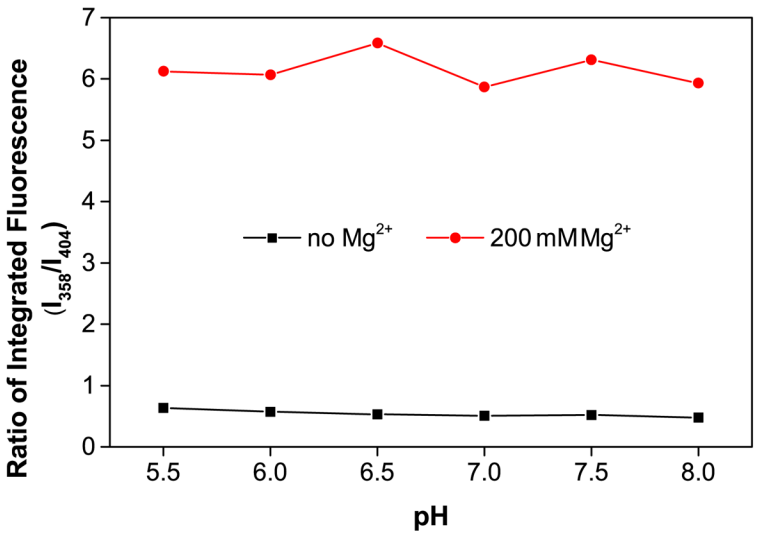

Figure S3. Fluorescence ratio ($I\lambda_1/I\lambda_2$) of a 0.5 μM solution of BCN-clicked sensor in aqueous buffer as a function of pH (50 mM buffer, 100 mM KCl, 25 °C), in the presence and absence of Mg^{2+}. Excitation wavelengths: $\lambda_1 = 358$ nm, $\lambda_2 = 404$ nm.

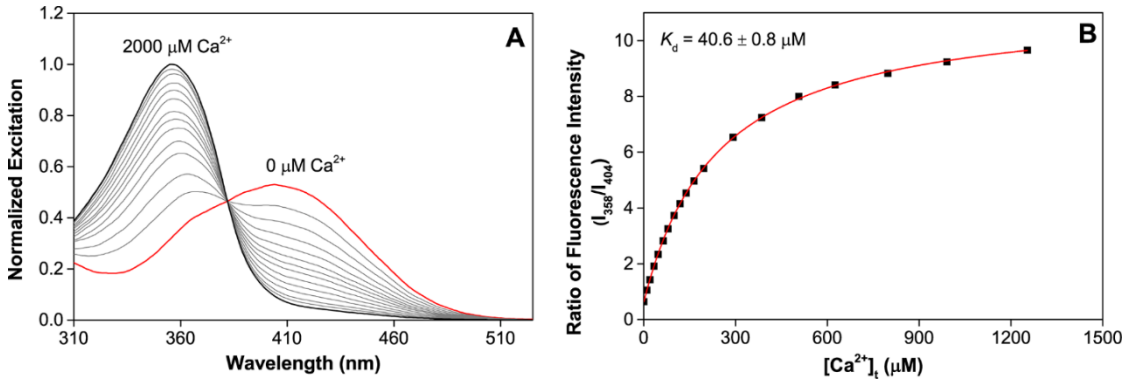

Figure S4. (A) Representative fluorescence excitation spectra of a 1 μM solution of BCN-activated sensor in aqueous buffer at pH 7.0, 25 °C, as a function of Ca^{2+} concentration. Emission wavelength: 595 nm. (B) Representative binding isotherm. Dissociation constant corresponds to the average of three independent titrations.

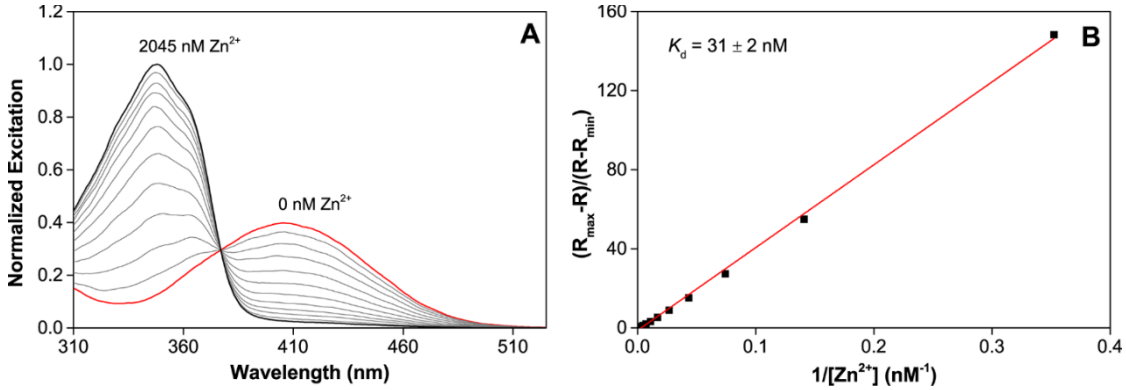

Figure S5. (A) Representative fluorescence excitation spectrum of a 0.5 μM solution of BCN-activated sensor in aqueous buffer at pH 7.0, 25 °C, as a function of Zn^{2+} concentration. Emission wavelength: 595 nm. (B) Representative double reciprocal plot for the change in fluorescence ratio as a function of free zinc concentration. Excitation wavelengths: λ_1 = 348 nm, λ_2 = 404 nm. $R=I_{348}/I_{404}$. Dissociation constant corresponds to the average of three independent titrations.

S1.2 Metal response of protein-anchored Mag-*S*-Tz

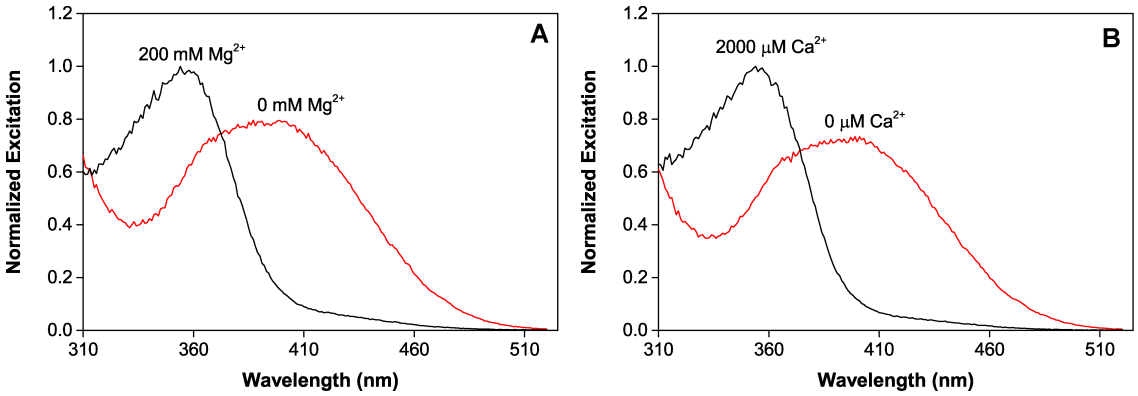

Figure S6. (A) Representative fluorescence excitation spectrum of a 0.5 μM solution of HaloTag-**Mag-*S*-Tz** in aqueous buffer at pH 7.0, 25 °C, before and after addition of Mg^{2+}. Emission wavelength λ_{em} = 595 nm. (B) Representative fluorescence excitation spectrum of a 0.5 μM solution of compound HaloTag-**Mag-*S*-Tz** in aqueous buffer at pH 7.0, 25 °C, as a function of calcium concentration. Emission wavelength: 595 nm.

S1.3 Kinetic studies of the reaction of Mag-*S*-Tz with BCN or with HaloTag-BCN

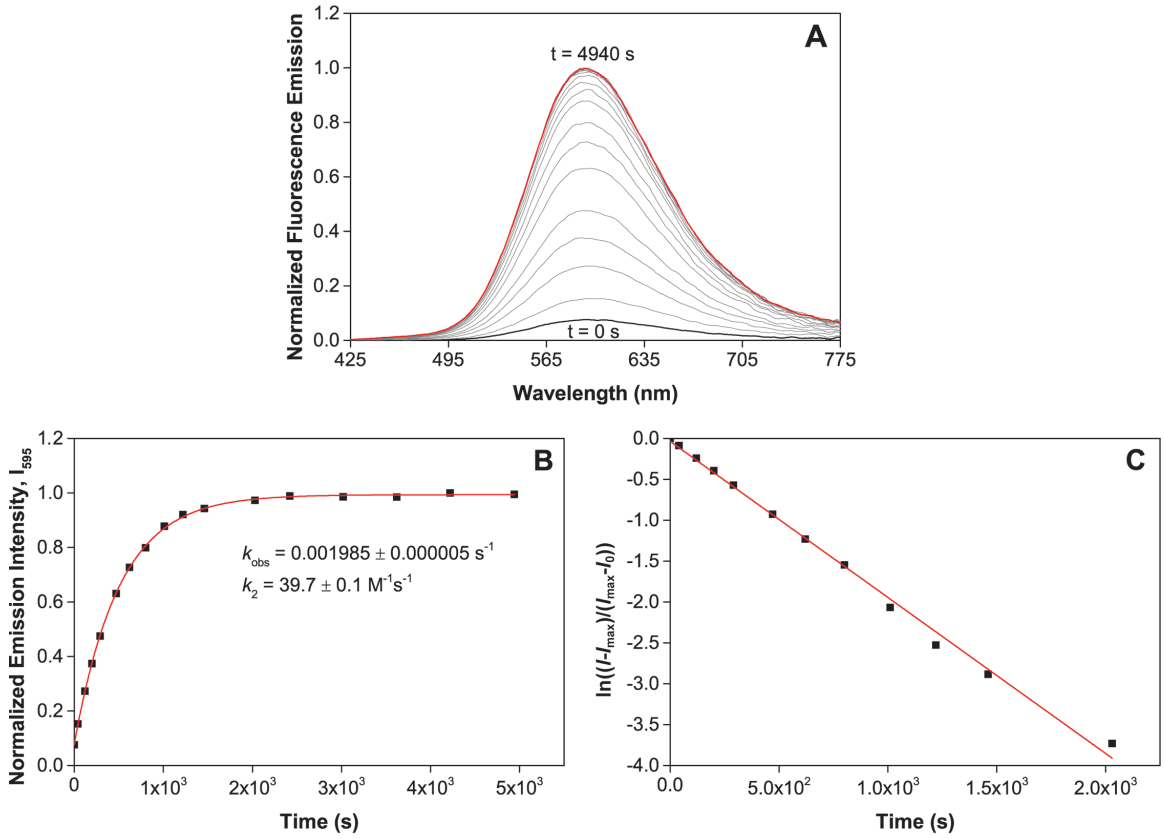

Figure S7. (A) Fluorescence emission spectra of 1 µM **Mag-*S*-Tz** treated with 50 µM of BCN in aqueous buffer at pH 7.0, 25 °C, as a function of time. Excitation wavelength: 404 nm. (B) Kinetic profile of the reaction of compound **Mag-*S*-Tz** with BCN monitored at 595 nm. Rate constants correspond to the averages of two independent measurements. (C) Linearized integrated rate law for a pseudo first order reaction.

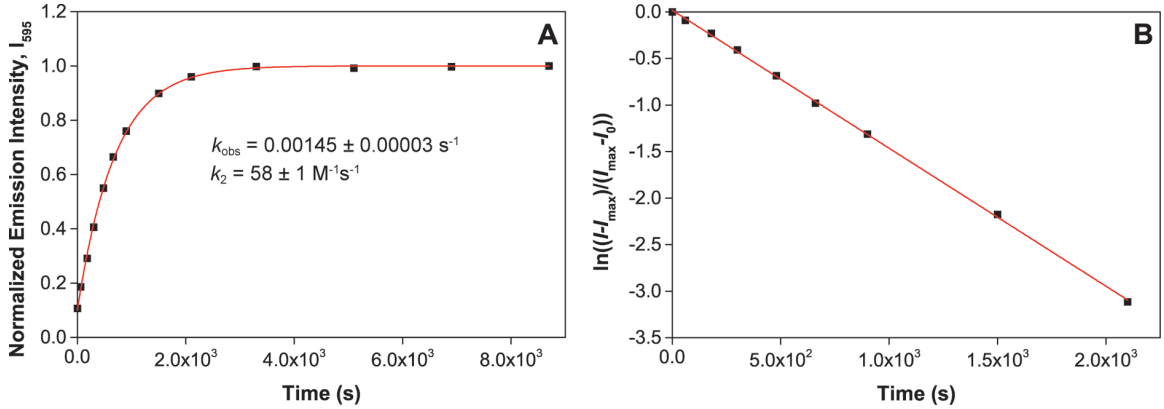

Figure S8. (A) Kinetic profile for the reaction of 0.5 µM **Mag-*S*-Tz** with 25 µM of BCN in aqueous buffer at pH 7.0, 37 °C, monitored at 595 nm (λ_{exc}= 404 nm). (B) Linearized integrated rate law for a pseudo first order reaction.

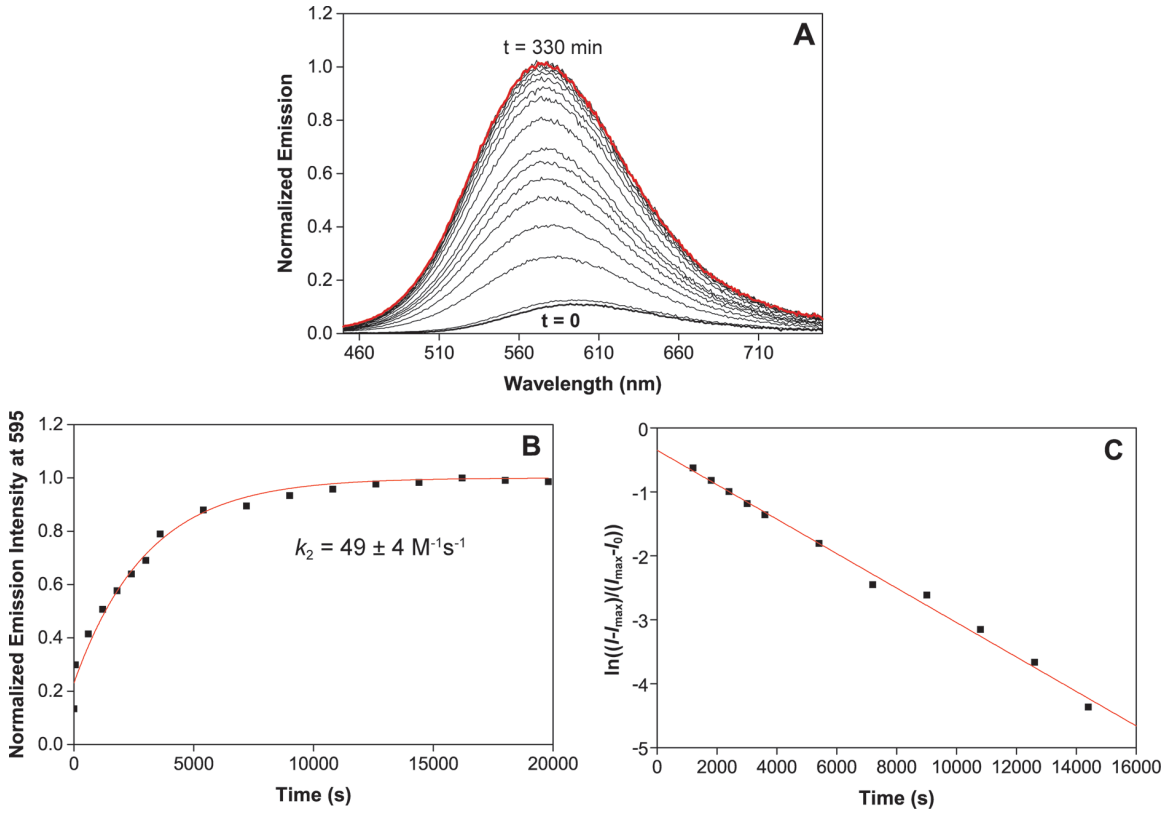

Figure S9. (A) Fluorescence emission spectra of 1 µM **Mag-*S*-Tz** treated with 7 µM of BCN-HaloTag in aqueous buffer at pH 7.0, 25 °C, as a function of time. Excitation wavelength: 404 nm. (B) Kinetic profile of the reaction monitored at 595 nm. (C) Linearized integrated rate law for a pseudo first order reaction.

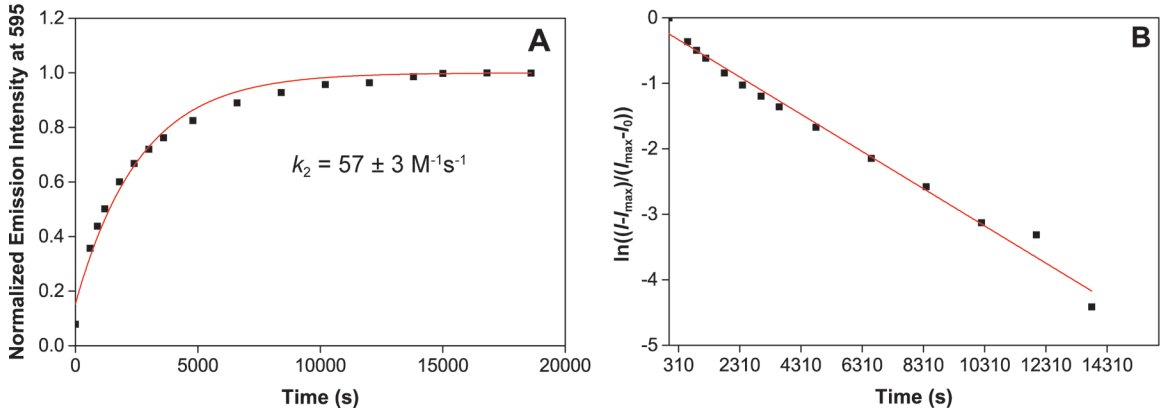

Figure S10. (A) Kinetic profile for the reaction of 1 µM **Mag-*S*-Tz** with ~7 µM BCN-HaloTag in aqueous buffer at pH 7.0, 37 °C, monitored at 595 nm (λ_{exc}= 404 nm). (B) Linearized integrated rate law for a pseudo first order reaction.

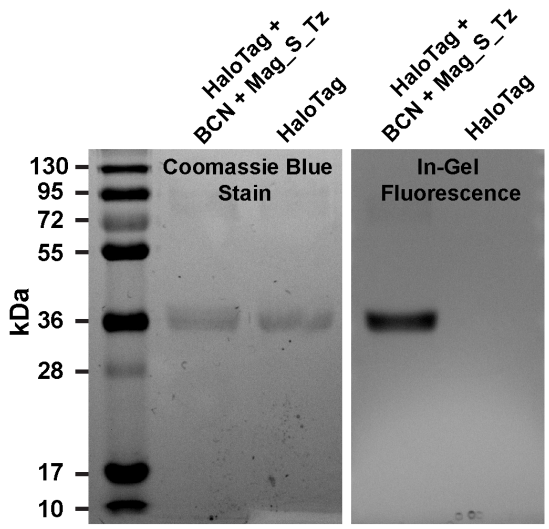

Figure S11. SDS-PAGE of HaloTag and HaloTag-**Mag-*S*-Tz**. Analysis was performed using Coomassie blue stain to label all protein and UV illumination of the gel to detect HaloTag-**Mag-*S*-Tz**.

S1.4 Fluorescence imaging

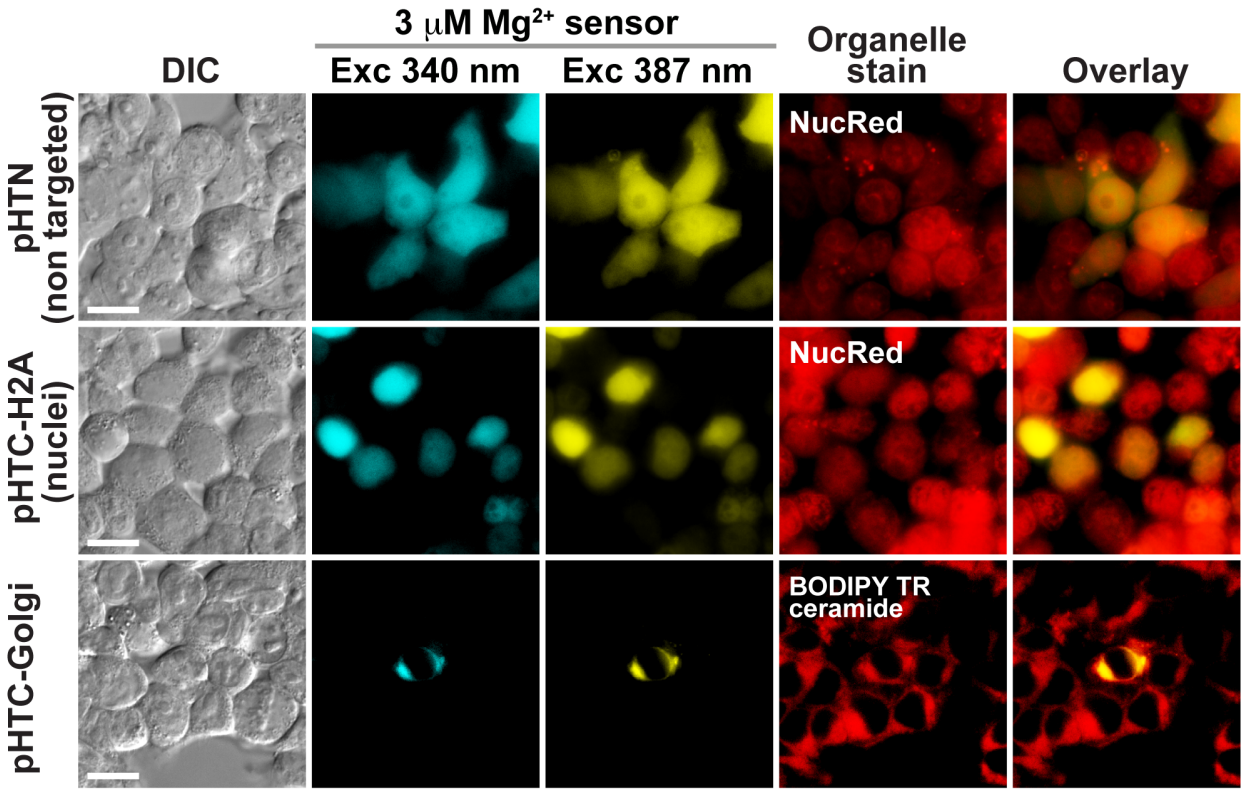

Figure S12. Fluorescence microscopy images of live HEK 293T cells transiently expressing HaloTag fusion proteins in the whole cell body (top row), in the nucleus (middle) or in the Golgi (bottom), labeled via two-step strategy comprising treatment with BCN-Cl ligand followed by **Mag-*S*-Tz-AM**. Fluorogenic reaction between the protein-anchored alkyne moiety and the tetrazine-functionalized sensor leads to fluorescence activation in the targeted compartment. Two pseudo-colored images are provided for the sensor, corresponding to excitation at two different wavelengths employed for excitation ratiometric imaging. Scale bar = 10 μm.

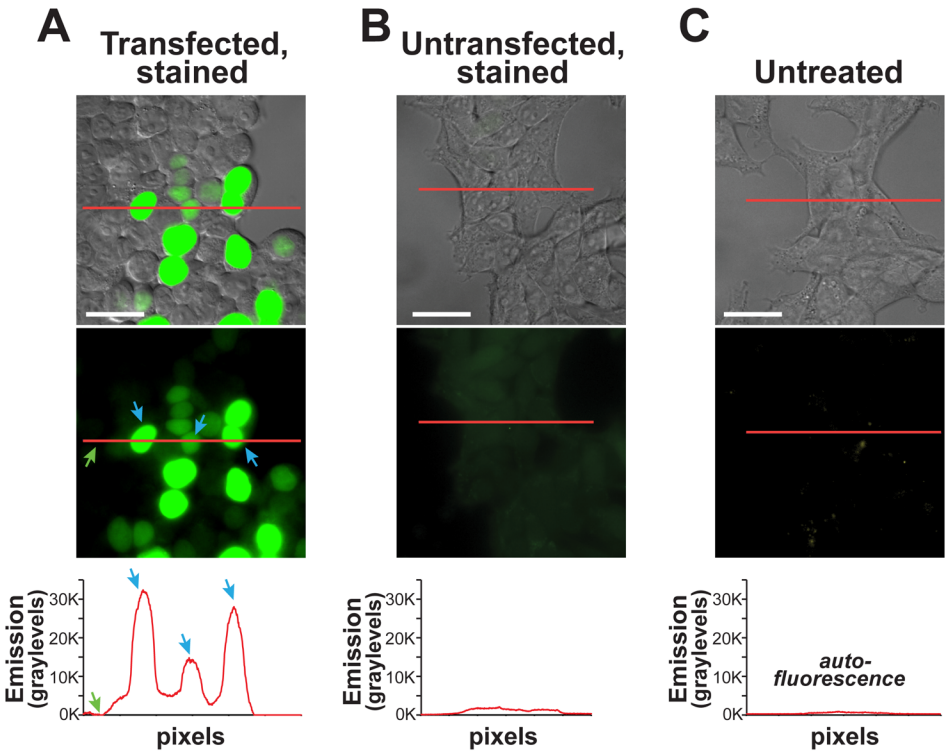

Figure S13. Fluorescence microscopy images of (A) cells transiently expressing HaloTag-H2A in the nucleus, stained with **Mag-*S*-Tz** via two-step protocol; (B) non-transfected cells, stained with **Mag-*S*-Tz**; and (C) untreated cells. The fluorescence intensity in the nuclei of cells along the trace transiently expressing the protein (blue arrows) is significantly enhanced as a product of the fluorogenic reaction. The fluorescence intensity from non-transfected cells in the same plate (green arrows, along the same trace) is not significantly higher than the autofluorescence detected in untreated cells in (C). Scale bar = 20 μm.

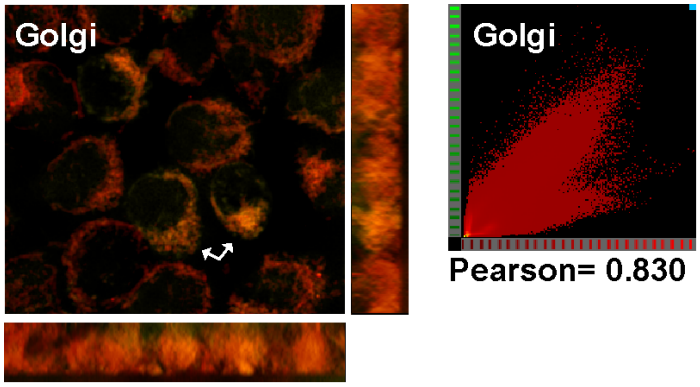

Figure S14. Image overlay and 2-D histograms showing the co-localization of Golgi-specific stain BODIPY TR Ceramide and **Mag-*S*-Tz** (loaded as AM ester) activated in the Golgi of live HEK 293T cells. Magnesium dye is pseudo-colored in yellow, whereas the Golgi stain is pseudo-colored in red. The analysis was conducted over the cell volume, reconstructed from a z-stacked series of images. White arrows indicate the cells transiently expressing pHTC-Golgi that were used to generate the 2-D histogram.

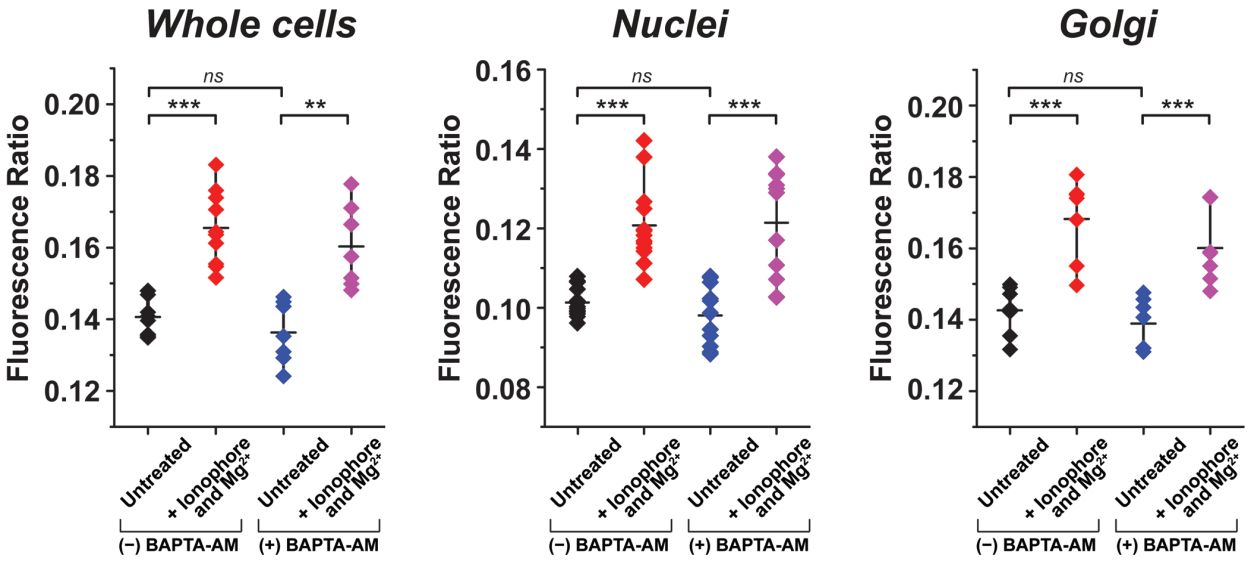

Figure S15. Fluorescence ratio of sensor **Mag-*S*-Tz** activated in various compartments of HEK 293T cells, treated with 30 mM $MgCl_2$ and 4-Br-A-23187 after treatment with intracellular calcium chelator BAPTA-AM (10 μM for nuclei and Golgi, 25 μM for whole cells) to rule out possible interference from Ca^{2+} in the detection of Mg^{2+}. Fluorescence Ratio = Intensity at 340 nm excitation/ Intensity at 387 nm excitation. ***$P \leq 0.001$; **$P \leq 0.01$; *ns* $P > 0.05$; *t*-test.

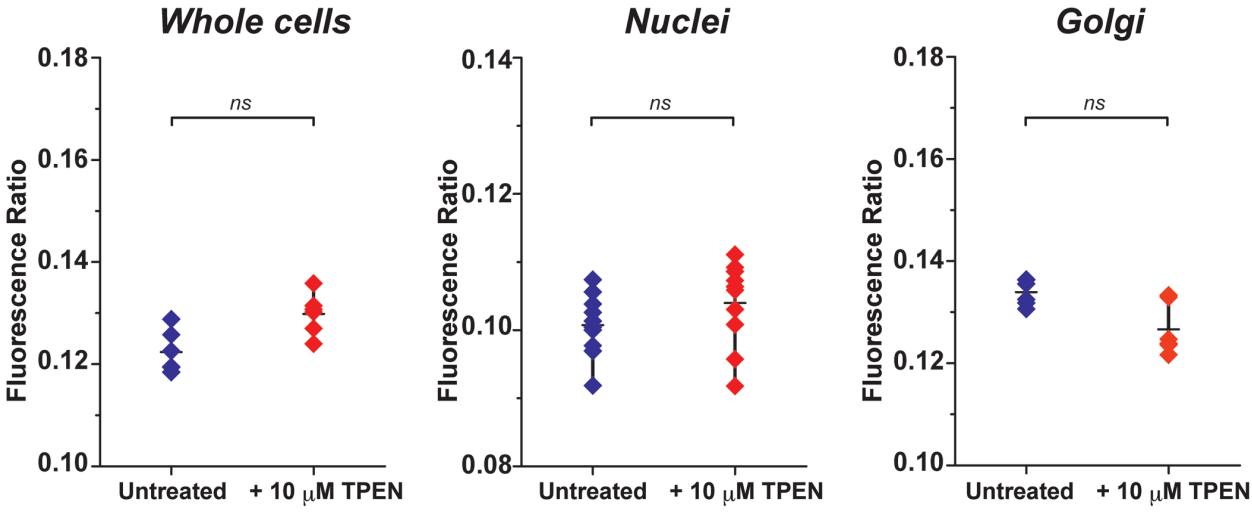

Figure S16. Fluorescence ratio of sensor **Mag-*S*-Tz** activated in various compartments of HEK 293T cells, before and after treatment with 10 μM intracellular chelator TPEN to rule out possible interference from Zn^{2+} in the detection of basal Mg^{2+}. Fluorescence Ratio = Intensity at 340 nm excitation/ Intensity at 387 nm excitation. *ns* $P > 0.05$; *t*-test.

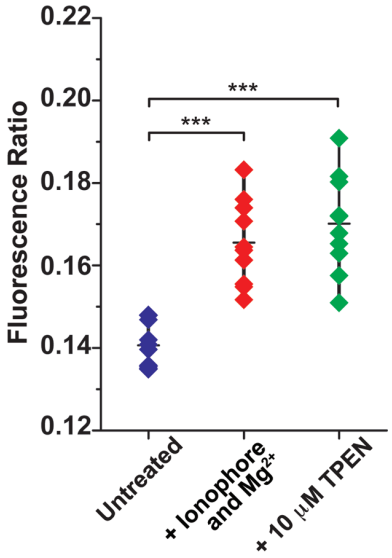

Figure S17. Fluorescence ratio of sensor **Mag-*S*-Tz** activated over the whole cell body of HEK 293T cells, before and after treatment with exogenous $MgCl_2$ and ionophore 4-Br-A-23187, followed by treatment with 10 μM intracellular chelator TPEN. The experiment rules out interference from Zn^{2+} in the detection of changes in intracellular Mg^{2+}, caused by possible mobilization of Zn^{2+} by the ionophore. Fluorescence Ratio = Intensity at 340 nm excitation/ Intensity at 387 nm excitation. ***$P \leq 0.001$; *t*-test

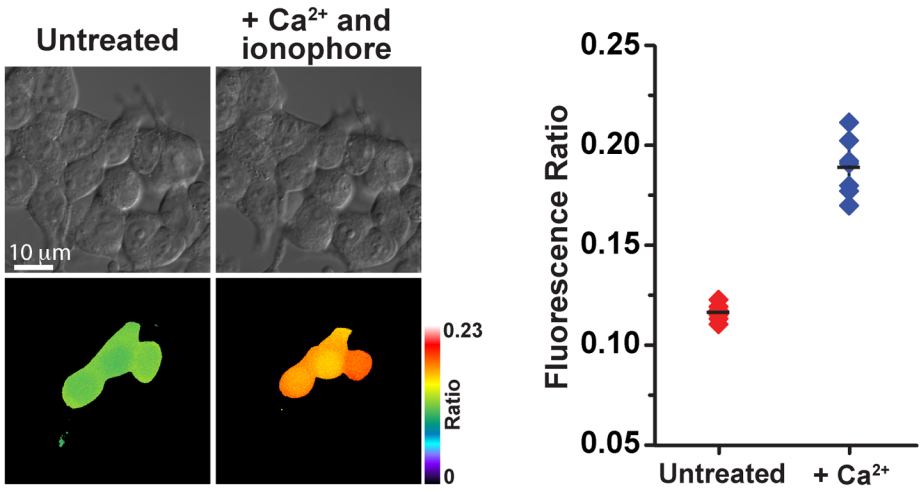

Figure S18. Ratiometric microscopy imaging of Ca^{2+} with sensor **Mag-*S*-Tz** (loaded as AM ester) activated intracellularly in HEK 293T cells expressing non-targeted HaloTag. Left: fluorescence ratio images before and after treatment with 10 mM Ca^{2+} and 10 μM ionomycin. Right: plots showing the change in fluorescence ratio that reflect the increase in intracellular Ca^{2+} concentration mediated by the ionophore. Fluorescence Ratio = Intensity at 340 nm excitation/ Intensity at 387 nm excitation.

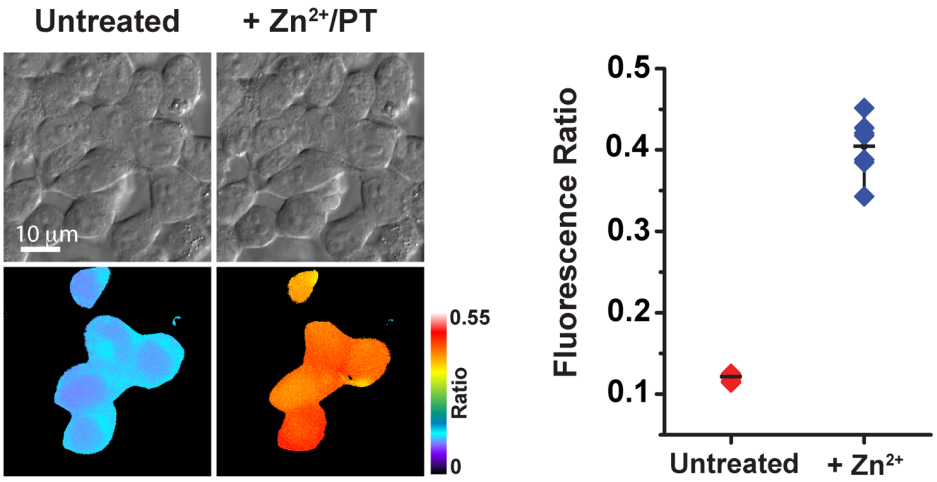

Figure S19. Ratiometric microscopy imaging of Zn^{2+} with sensor **Mag-*S*-Tz** (loaded as AM ester) activated intracellularly in HEK 293T cells expressing non-targeted HaloTag. Left: fluorescence ratio images before and after treatment with 50 µM Zn^{2+} in a one-to-one ratio with pyrithione. Right: plots showing the change in fluorescence ratio that reflect the increase in intracellular Zn^{2+} levels mediated by the ionophore. Fluorescence Ratio = Intensity at 340 nm excitation/ Intensity at 387 nm excitation.

S1.5 Cell viability studies

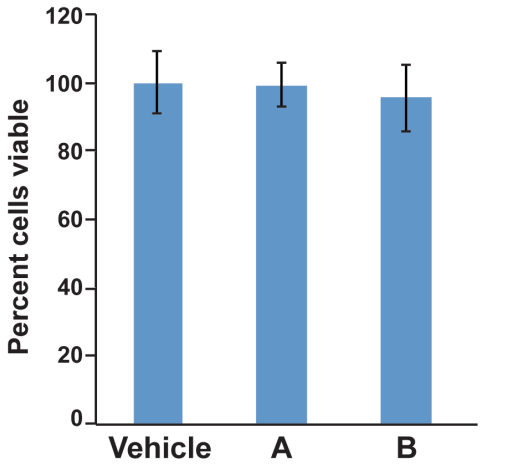

A: 10 µM BCN-Cl + 3 µM Mag-S-Tz
B: 10 µM BCN-Cl + 3 µM Mag-S-Tz,
+ 30 µM Ionophore and 30 mM Mg^{2+}

Figure S20. Viability of HEK 293T cells transiently expressing Halotag-H2A exposed to labeling protocol with BCN-Cl followed by **Mag-*S*-Tz-AM**, and treated with exogenous Mg^{2+} and ionophore 4-Br-A-23187.

S2. Synthetic procedures

S2.1 Synthesis of *tert*-butyl 2-(bromomethyl)thiazole-5-carboxylate, 1

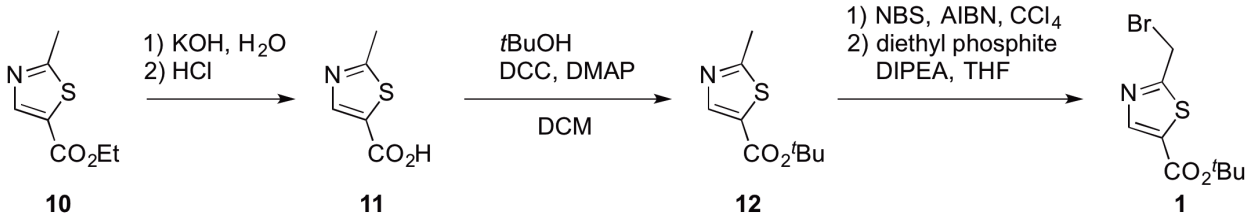

Synthesis of 2-methylthiazole-5-carboxylic acid, 11

A solution of ethyl 2-methylthiazole-5-carboxylate[1] (600mg, 3.50 mmol) in methanol (4 mL) was treated with aqueous potassium hydroxide (4 mL, 1.2 M, 4.8 mmol) and stirred at room temperature overnight. The solution was cooled to 0 °C and acidified with aqueous hydrochloric acid (1M) to pH 2 to yield a grey precipitate. The precipitate was collected by filtration, washed with water and dried under vacuum to give acid **11** as a grey solid (350 mg, 70%, R_f = 0.30 in 10:1 DCM:MeOH). M.p. 207-208 °C. ^{1}H NMR (400 MHz, DMSO-d_6, δ) 13.40 (s, 1H), 8.17 (s, 1H), 2.70 (s, 3H). ^{13}C{^{1}H} NMR (100 MHz, DMSO-d_6, δ) 171.8, 162.1, 147.6, 130.0, 19.4. ESI-MS (m/z): $[M+H]^+$ calcd for $C_5H_5NO_2S$, 142.0; found 142.3.

Synthesis of *tert*-butyl 2-methylthiazole-5-carboxylate, 12

A suspension of compound **11** (716 mg, 5 mmol) and DMAP (31 mg, 0.25 mmol) in dry dichloromethane (40 mL) was cooled to 0 °C and was added a solution of *N*,*N*'-dicyclohexylcarbodiimide (1.238g, 6 mmol) in dichloromethane (10 mL) at 0 °C over 10 min. The mixture was stirred at 0 °C for 10 min followed by addition of *t*-butanol and the reaction mixture was allowed to stir at room temperature overnight. The solid was filtered off and the filtrate was concentrated *in vacuo*. The residue was purified by column chromatography on silica gel (1:10 EtOAc:hexanes) to give product **12** as a yellow liquid (720 mg, 72 %, R_f = 0.35 in 1:9 EtOAc:hexanes). ^{1}H NMR (400 MHz, $CDCl_3$, δ) 8.13 (s, 1H), 2.72 (s, 3H), 1.56 (s, 9H). ^{13}C{^{1}H}

NMR (100 MHz, $CDCl_3$, δ) 171.5, 160.6, 147.6, 131.0, 82.5, 28.2, 19.7. ESI-MS (m/z): $[M+H]^+$ calcd for $C_9H_{13}NO_2S$, 200.1; found 200.0.

Synthesis of *tert*-butyl 2-(bromomethyl)thiazole-5-carboxylate, 1

A mixture of compound **12** (720 mg, 3.61 mmol), *N*-bromosuccinimide (1.608 g, 9.03 mmol) and azobisisobutyronitrile (237 mg, 1.45 mmol) in dry carbon tetrachloride (35 mL) was stirred at 50 °C under inert atmosphere overnight. The reaction mixture was cooled down to room temperature and the solid was filtered off. The filtrate was concentrated and redissolved in ethyl acetate (30 mL). The resulting organic solution was washed with aqueous $Na_2S_2O_3$ and brine, dried with Na_2SO_4 and concentrated *in vacuo*. The residue was dissolved in dry tetrahydrofuran (4 mL) and cooled to 0 °C. Diethylphosphite (748 mg, 5.42 mmol) and *N*,*N*-diisopropylethylamine (701 mg, 5.42 mmol) were added and the reaction mixture was stirred at 0 °C under inert atmosphere for 1.5 h. The reaction mixture was diluted with ether and washed with aqueous hydrochloric acid (1M) and brine, dried with $MgSO_4$ and concentrated *in vacuo*. The residue was purified by column chromatography on silica gel (1:10 EtOAc:hexanes) to give thiazole **1** as a pale yellow liquid (300 mg, 30%, R_f = 0.55 in 9:1 hexanes:EtOAc). ^{1}H NMR (400 MHz, $CDCl_3$, δ) 8.21 (s, 1H), 4.68 (s, 2H), 1.56 (s, 9H). $^{13}C\{^1H\}$ NMR (100 MHz, $CDCl_3$, δ) 170.7, 160.2, 147.8, 133.5, 83.3, 28.3, 26.4. ESI-MS (m/z): $[M+H]^+$ calcd for $C_9H_{12}BrNO_2S$, 278.0; found 277.9.

S2.2 Synthesis of BCN-Cl

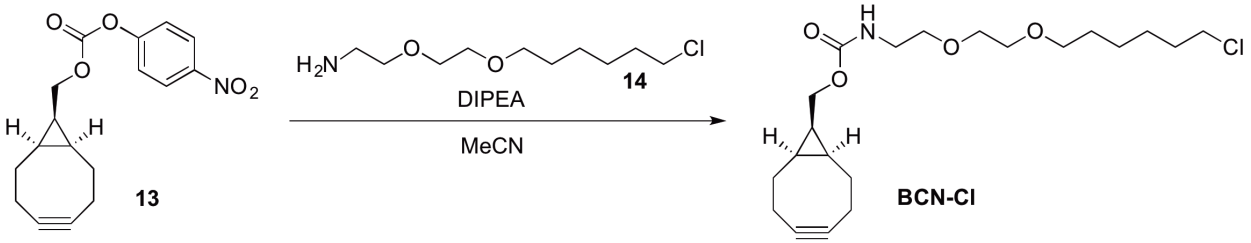

A solution of compound **13**[2] (20 mg, 0.063 mmol), amine **14**[3] (28 mg, 0.126 mmol) and diisopropylethylamine (24 mg, 0.190 mmol) in acetonitrile (1.0 mL) was stirred at room

temperature overnight. The reaction mixture was concentrated and the residue was redissolved in EtOAc (5.0 mL). The resulted organic solution was washed with aqueous K_2CO_3 (10% w/w), dried over Na_2SO_4 and concentrated *in vacuo*. The residue was purified by column chromatography on silica gel (5:1 Hexanes/EtOAc) to give **BCN-Cl** as a colorless oil (19 mg, 75%, R_f = 0.26 in 3:1 Hexanes/EtOAc). ^{1}H NMR (400 MHz, $CDCl_3$, δ): 5.17 (s, 1H), 4.14 (d, *J* = 8.0 Hz, 2H), 3.62-3.59 (m, 2H), 3.57-3.51 (m, 6H), 3.47-3.44 (m, 2H), 3.39-3.35 (m, 2H), 2.32-2.18 (m, 6H), 1.80-1.73 (m, 2H), 1.64-1.52 (m, 4H), 1.49-1.30 (m, 5H), 0.96-0.91 (m, 2H). ^{13}C{^{1}H} NMR (100 MHz, $CDCl_3$, δ):156.9, 98.9, 71.4, 70.5, 70.23, 70.17, 62.8, 45.2, 40.9, 32.7, 29.6, 29.2, 26.8, 25.6, 21.6, 20.2, 17.9. ESI-MS (m/z): $[M+Na]^+$ calcd for $C_{21}H_{34}ClNO_4$, 422.2; found 422.1.

S3. Metal dissociation constants from spectroscopic studies

Apparent K_d values for Mg^{2+} dissociation were obtained using equation S1,[4] where R is the ratio of fluorescence intensity upon excitation at two wavelengths ($R=I\lambda_1/I\lambda_2$), R_{min} is the fluorescence ratio for the metal-free sensor, R_{max} is the fluorescence ratio of the metal-saturated sensor, and S_{f2} and S_{b2} are proportionality coefficients for the fluorescence emission intensity of the metal-free and -bound forms of the sensor, respectively, upon excitation at λ_2.

$$[Mg^{2+}] = K_d \frac{R - R_{min}}{R_{max} - R} \frac{S_{f2}}{S_{b2}} \quad \text{(S1)}$$

Linear fit of plots of $(R_{max}-R)/(R-R_{min})$ vs. $1/[Mg^{2+}]$ were employed, using the approximation $[Mg^{2+}] \approx [Mg^{2+}]_t$. Reported K_d values correspond to averages of three independent titrations.

Apparent K_d values for Ca^{2+} dissociation were obtained from non-linear plots of the fluorescence ratio R as a function of total Ca^{2+} concentration, $[Ca^{2+}]_t$, according to equation S2, with values of free calcium concentration, $[Ca^{2+}]$, obtained at each point by solving numerically equation S3.[5]

$$R = \frac{R_{\max}[Ca^{2+}] + R_{\min}(K_d S_{f2} / S_{b2})}{[Ca^{2+}] + (K_d S_{f2} / S_{b2})} \quad \text{(S2)}$$

$$[Ca^{2+}]^2 + ([Sensor]_t - [Ca^{2+}]_t + K_d)[Ca^{2+}] - K_d[Ca^{2+}]_t = 0 \quad \text{(S3)}$$

Zinc titrations were conducted using an EGTA-Zn^{2+} buffer system. Apparent K_d values for Zn^{2+} dissociation from the fluorescent indicator were obtained with equation S4,[4] using linear plots of $(R_{max}-R)/(R-R_{min})$ as a function of $1/[Zn^{2+}]$.

$$[Zn^{2+}] = K_d \frac{R - R_{\min}}{R_{\max} - R} \frac{S_{f2}}{S_{b2}} \quad \text{(S4)}$$

Free concentrations of zinc at each point of the titration were calculated from values of total zinc concentration, $[Zn^{2+}]_t$, and total EGTA concentration, $[EGTA]_t$, using an apparent binding constant for Zn^{2+}-EGTA of $\log K'_{ZnEGTA} = 8.24$ at pH 7.0. The latter was calculated from reported pK_a values of EGTA and stability constants of the zinc complex.[6]

S4. Kinetic studies

The rate constants k_{obs} for the pseudo-first order reactions of **Mag-*S*-Tz** with BCN, or with protein-anchored BCN (HaloTag-BCN), were obtained from non-linear plots of the fluorescence intensity versus time according to equation S5, where I is fluorescence intensity of reaction mixture at 595 nm, I_0 is the initial fluorescence intensity of unreacted **Mag-*S*-Tz** at 595 nm, and I_{max} is the fluorescence intensity of the reaction product at 595 nm. The second order rate constant, k_2, was calculated from the pseudo-first order rate constant, k_{obs}.

$$I = I_{\max} - (I_{\max} - I_0) \cdot e^{-k_{obs}t} \quad \text{(S5)}$$

S5. Construction of targeting vectors

pHTC_HaloTag CMV-neo vector and pHTN_HaloTag CMV-neo vector were obtained from Promega. pmTurquoise2-golgi (Addgene plasmid # 36205), pmTurquoise2-Mito (Addgene plasmid # 36208), and pmTurquoise2-H2A (Addgene plasmid # 36207) were a gift from Dorus Gadella. [7 610] The golgi, mitochondria, and nucleus targeting vectors were prepared by appending

the HaloTag to the carboxy terminus of the respective targeting sequence. For preparation of pHTC_golgi the golgi-signaling sequence (first 61 nucleotides) of β-1,4-galactosyltransferase was amplified from pmTurquoise2-golgi using the primers listed below, which contained the *NheI* and *EcoRI* restriction site sequences. The PCR products were purified using a PCR purification kit (Qiagen), restriction enzyme digested with *NheI* and *EcoRI*, and ligated into digested pHTC_HaloTag CMV-neo vector. Similarly, pHTC-H2A was prepared by amplifying the full-length sequence of Histone protein H2A using the described method. Similarly, pHTC-H2A was prepared by amplifying the full-length sequence of Histone protein H2A using the described method. pCDNA3-4xMito-Halo was prepared by replacing the Ca^{2+} FRET sensing portion of pcCDNA3-4mtD3cpv with HaloTag. The mitochondria targeting sequence (4 repeats of cytochrome *c* oxidase subunit VIII) and pCDNA3 vector backbone were amplified from pcCDNA3-4mtD3cpv with *EcoRI* and *NotI* restriction site. HaloTag was amplified from pHTC with *EcoRI* and *NotI* restriction sites as well. The linear vector backbone and insert was digested with *EcoRI* and *NotI* and ligated together to make pCDNA3-4xMito-Halo. The construct sequences were verified by sequencing (Genewiz) and plasmids were purified prior to transfection using an Endo-Free Plasmid Maxi Kit (Qiagen). Below are the primers used with the restriction sites are underlined.

Golgi

FWD: ATAGCTAGCATGAGGCTTCGGGAGCCG

REV: ATAGAATTCCTGCAGCGGTGTGGAGACTC

Mitochondria

FWD-MITO: ATAGCGGCCGCTCGAGCATG

REV-MITO: ATAGAATTCGCTCACCATGGTGGCAAG

FWD-HALO: ATAGAATTCCCAACCACTGAGGATCTGTACTTTCAG

REV-HALO: ATAGCGGCCGCTTAACCGGAAATCTCCAGAGTAGACAGC

H2A

FWD: ATAGCTAGCATGTCGGGACGCGGCTTC

REV: ATAGAATTCTTTGCCTTTGGCCTTGTGGTG

S6. NMR spectroscopic data for new compounds

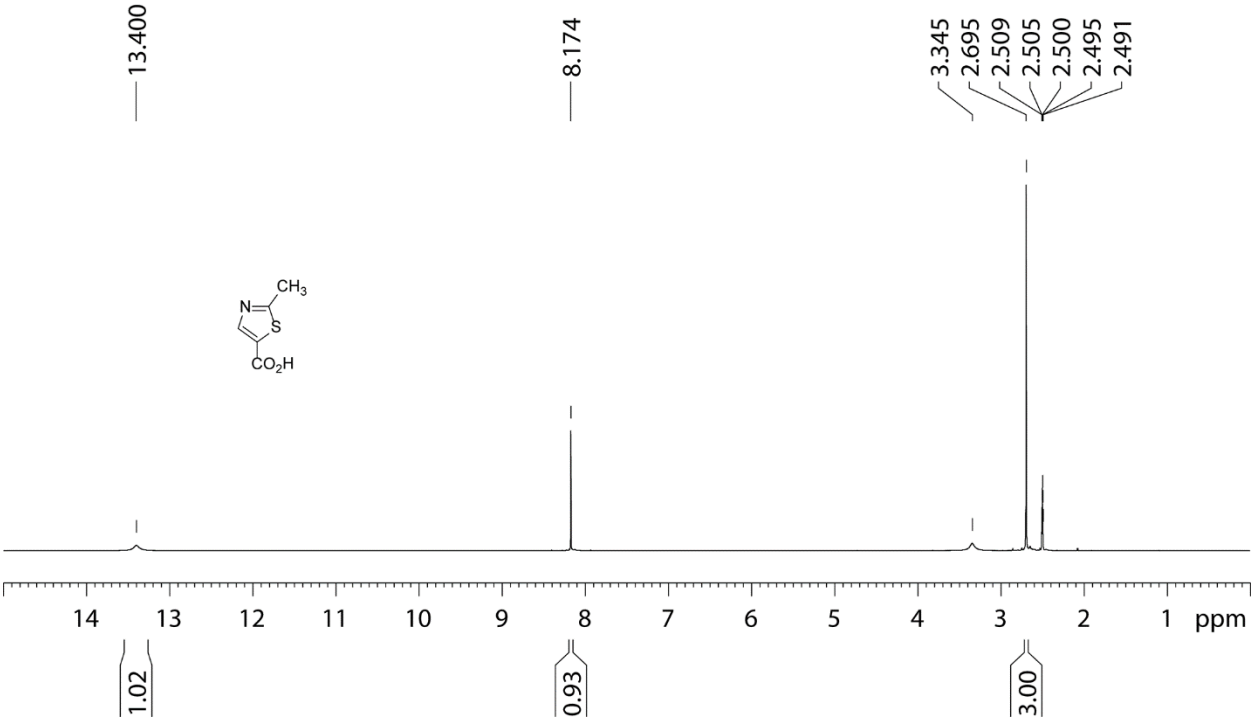

Figure S21. ^{1}H NMR spectrum of compound **11** in DMSO-d_6.

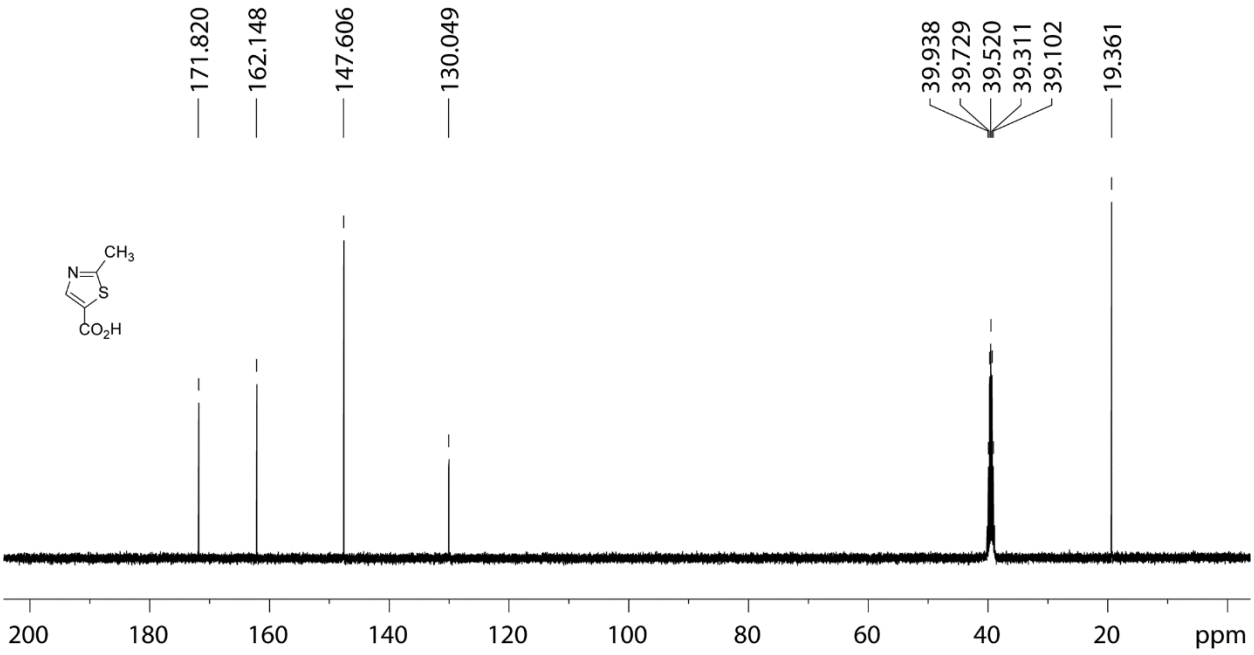

Figure S22. ^{13}C{^{1}H} NMR spectrum of compound **11** in DMSO-d_6.

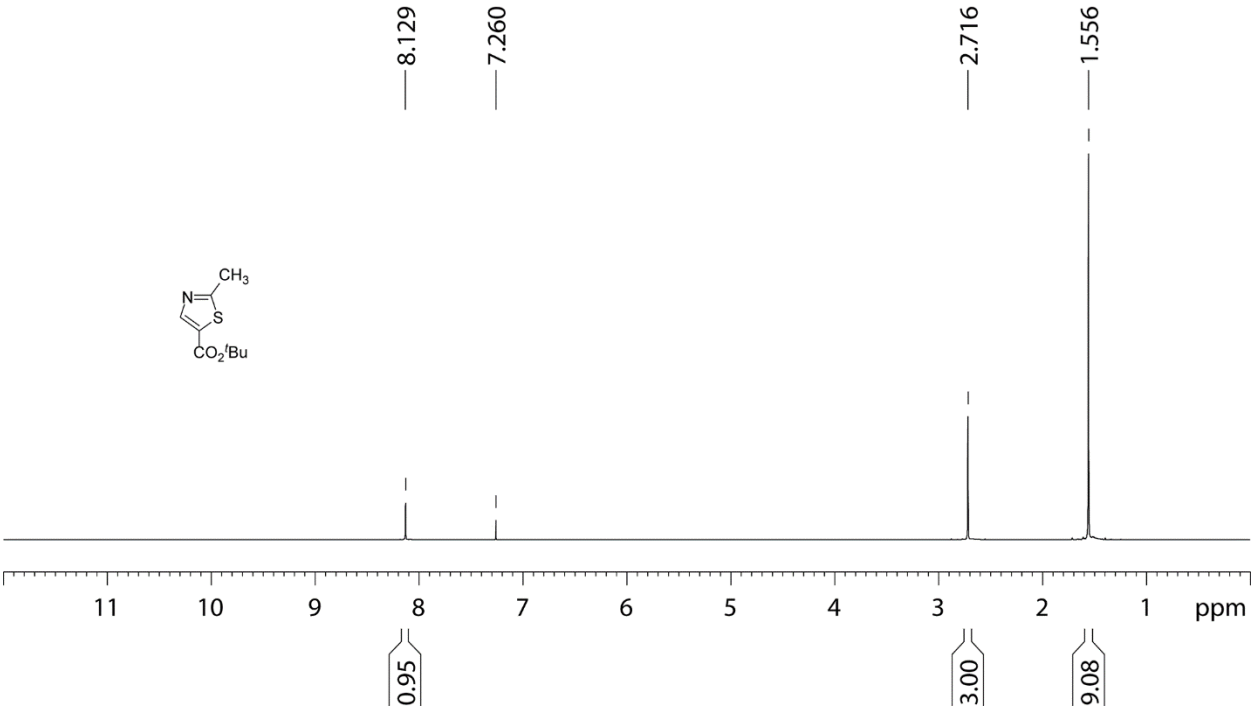

Figure S23. ^{1}H NMR spectrum of compound **12** in $CDCl_3$.

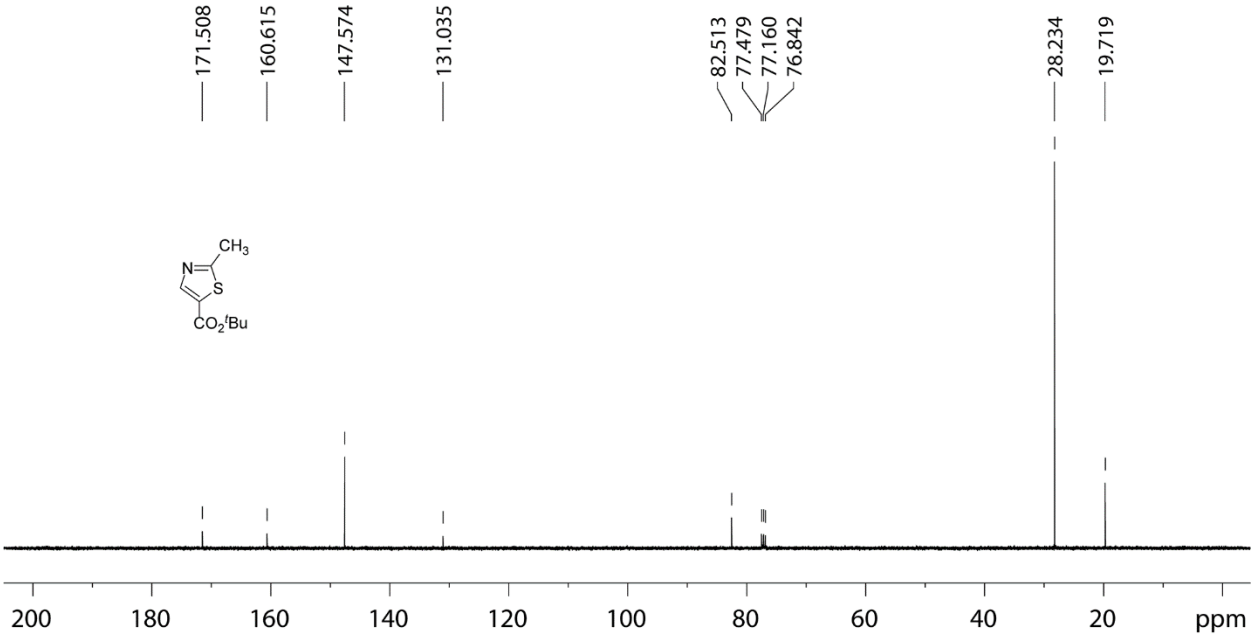

Figure S24. $^{13}C\{^{1}H\}$ NMR spectrum of compound **12** in $CDCl_3$.

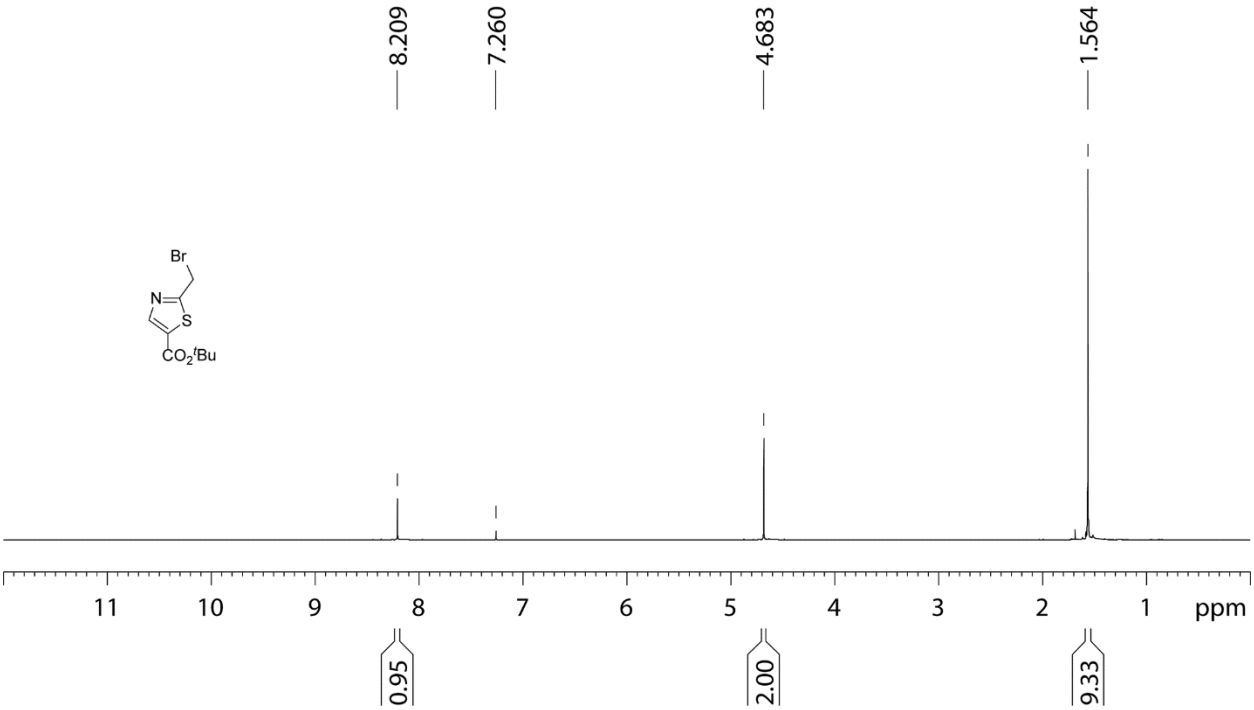

Figure S25. ^{1}H NMR spectrum of compound **1** in $CDCl_3$.

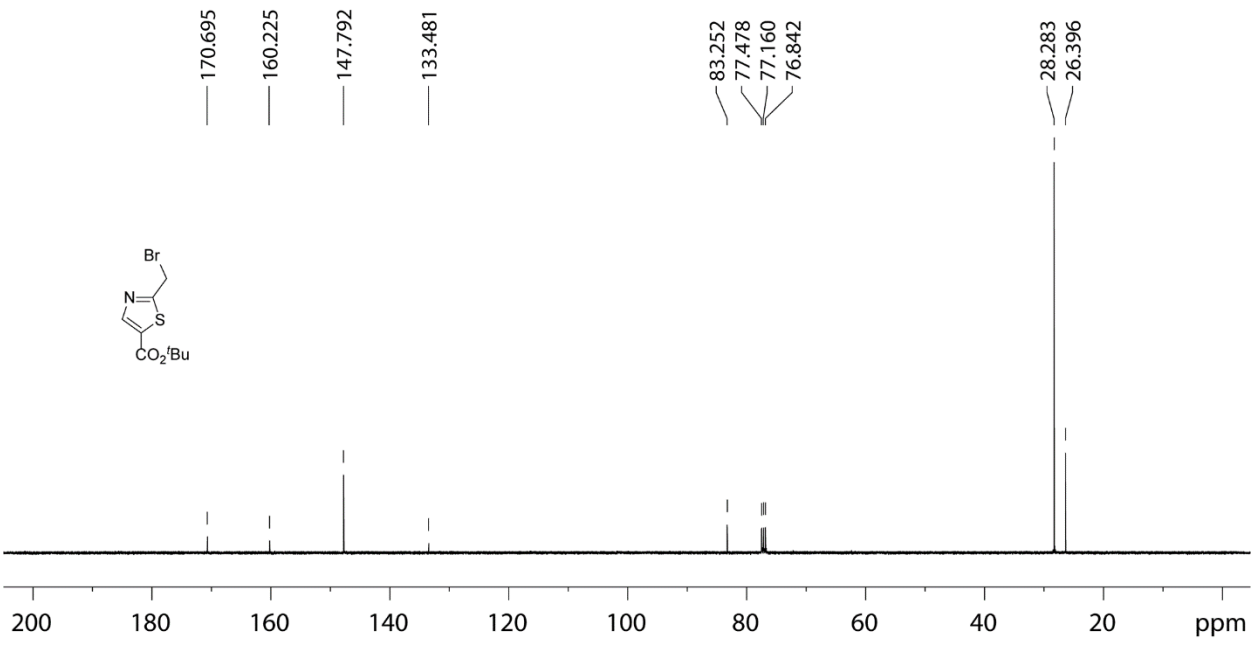

Figure S26. $^{13}C\{^{1}H\}$ NMR spectrum of compound **1** in $CDCl_3$.

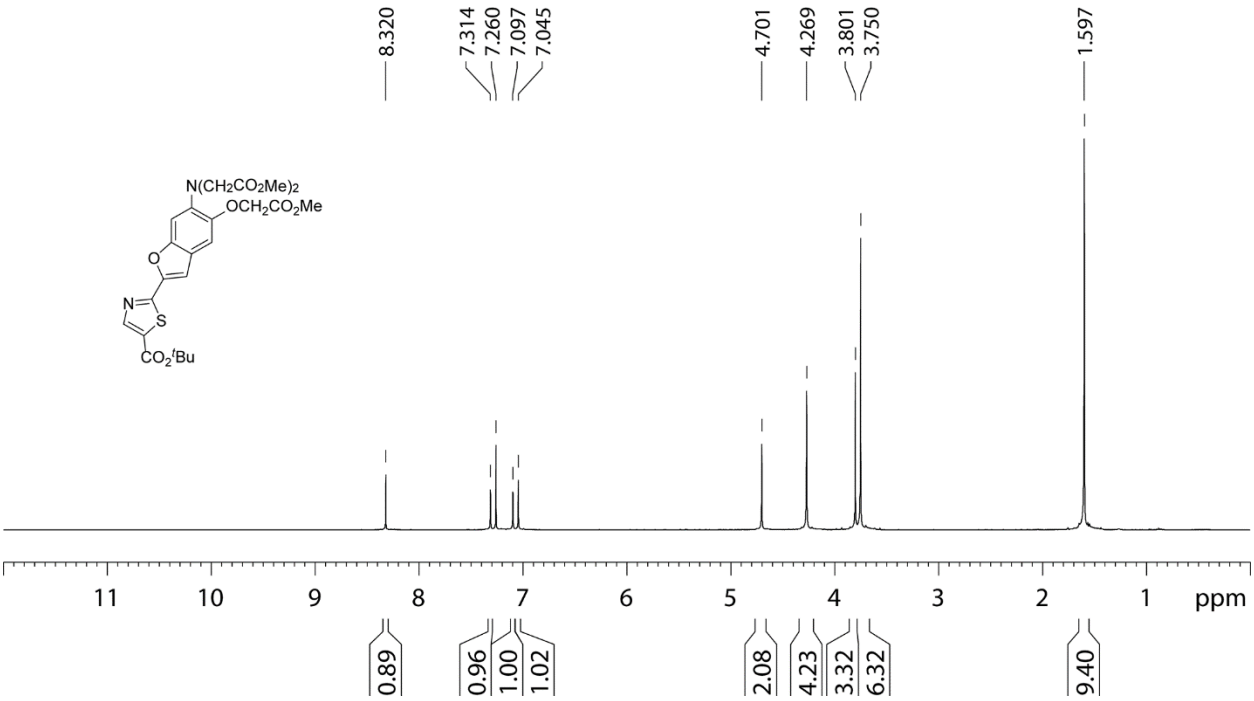

Figure S27. ^{1}H NMR spectrum of compound **3** in $CDCl_3$.

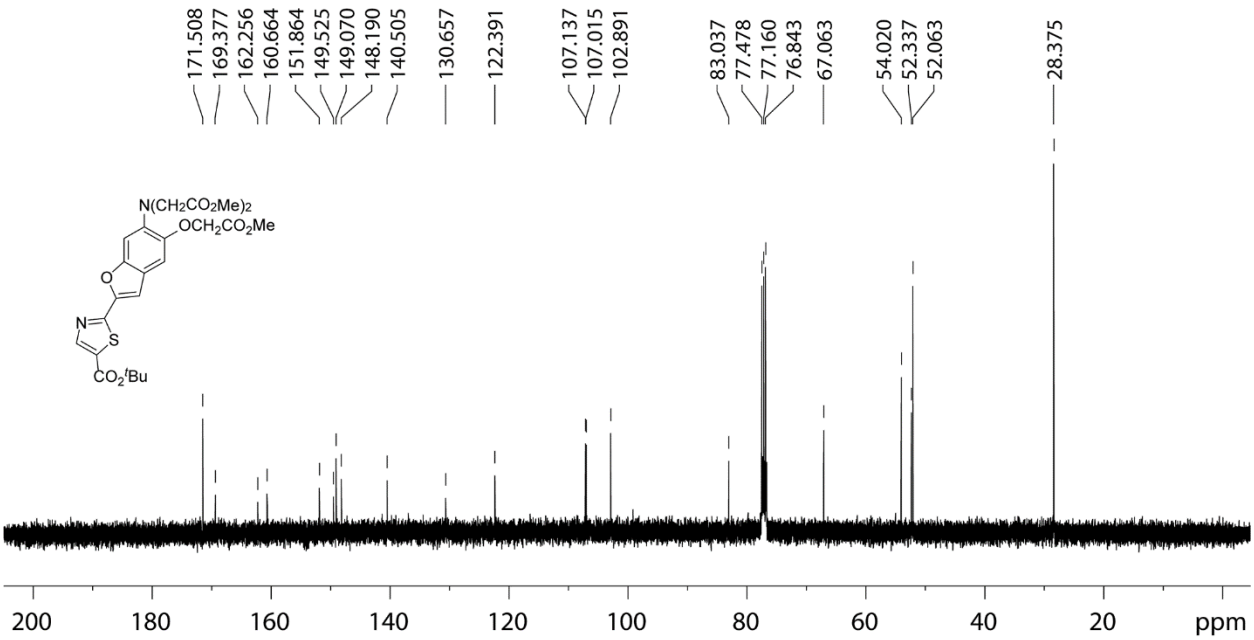

Figure S28. $^{13}C\{^{1}H\}$ NMR spectrum of compound **3** in $CDCl_3$.

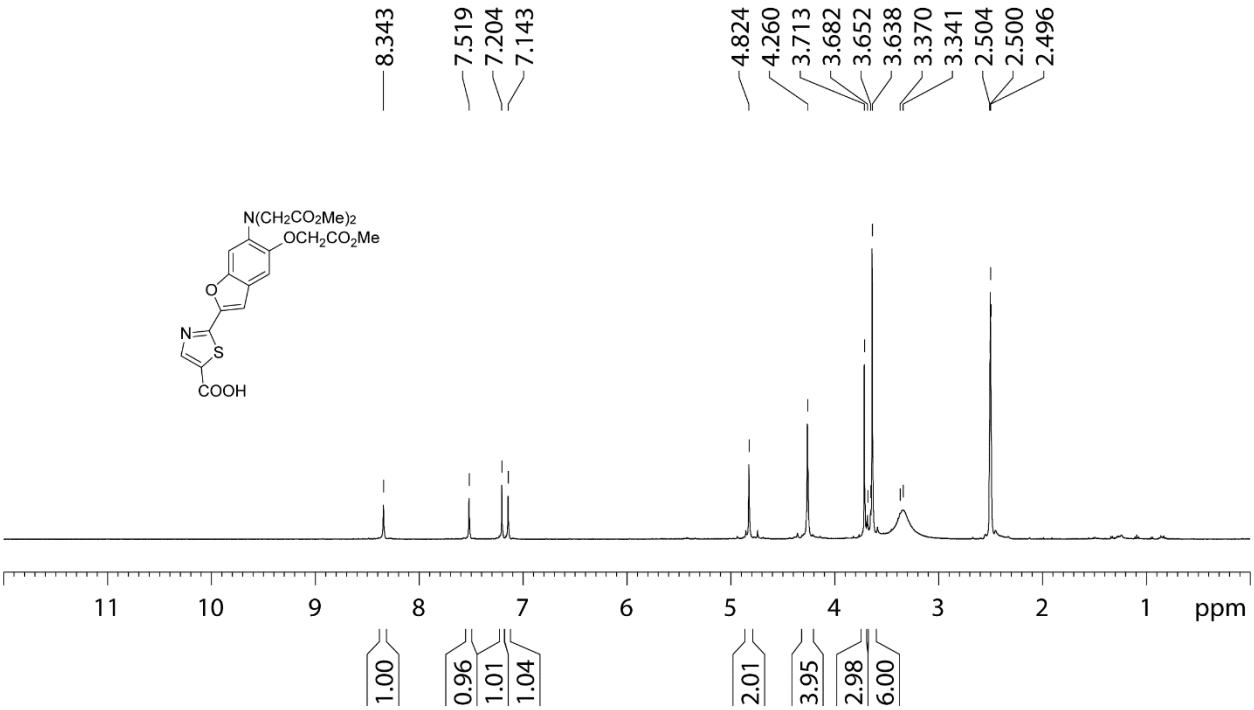

Figure S29. ^{1}H NMR spectrum of compound **4** in DMSO-d_6.

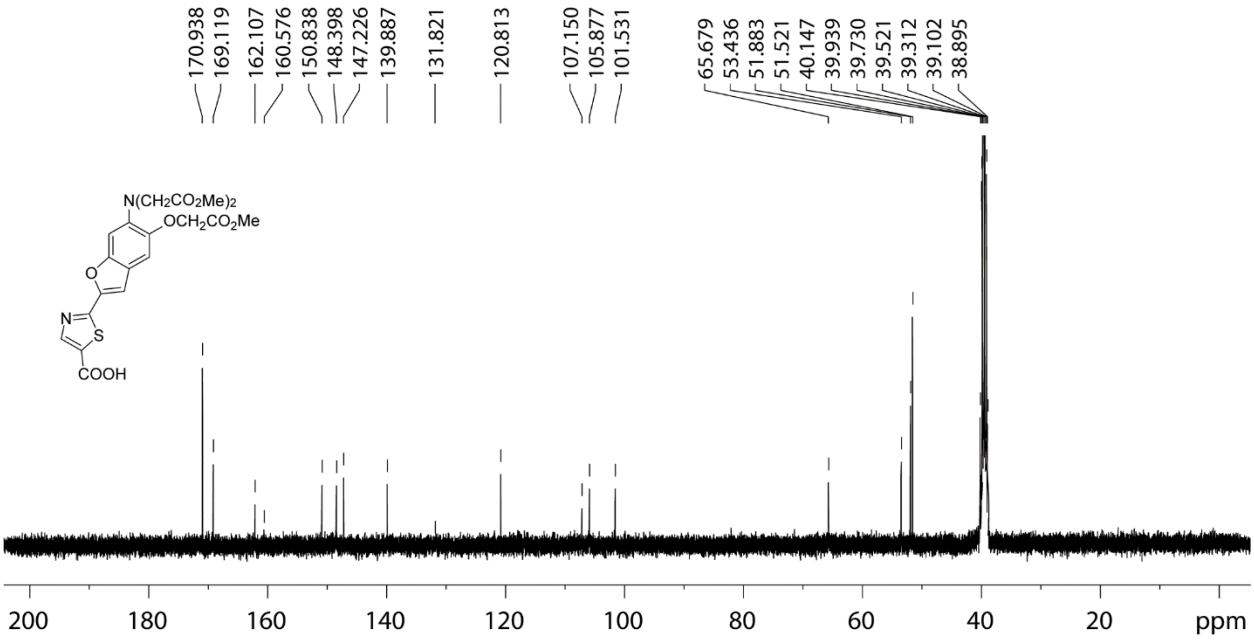

Figure S30. ^{13}C{^{1}H} NMR spectrum of compound **4** in DMSO-d_6.

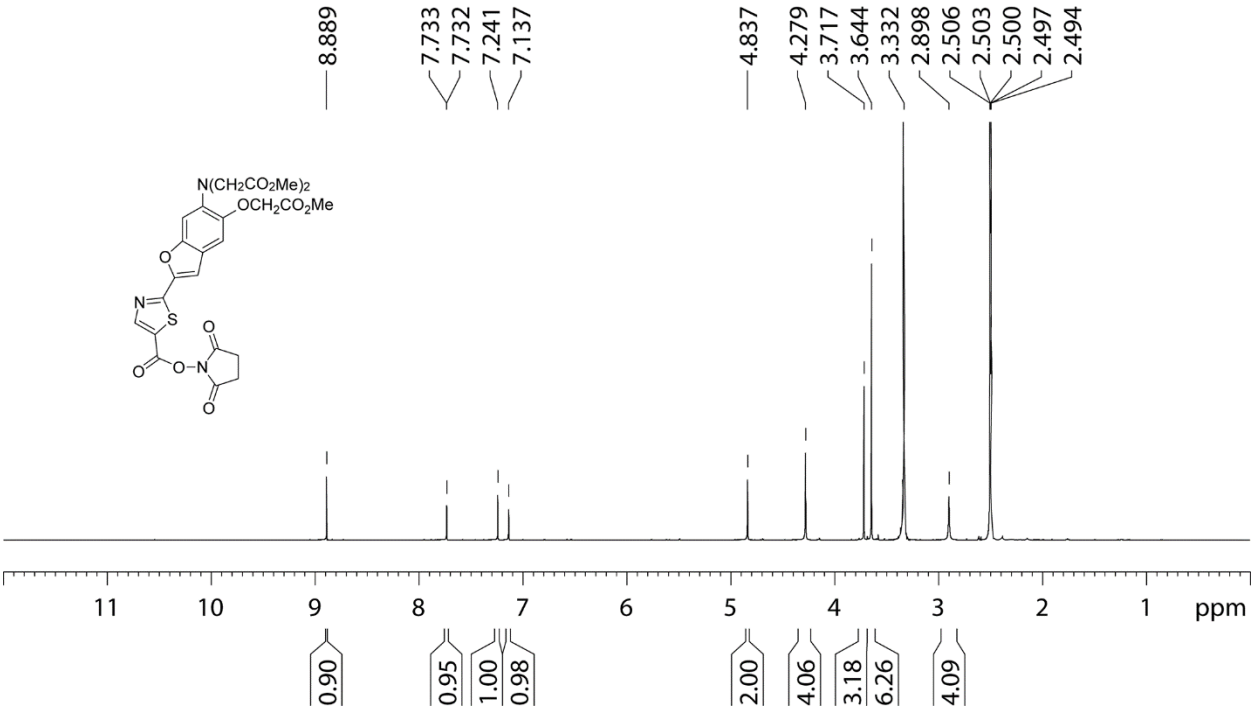

Figure S31. ^{1}H NMR spectrum of compound **5** in DMSO-d_6.

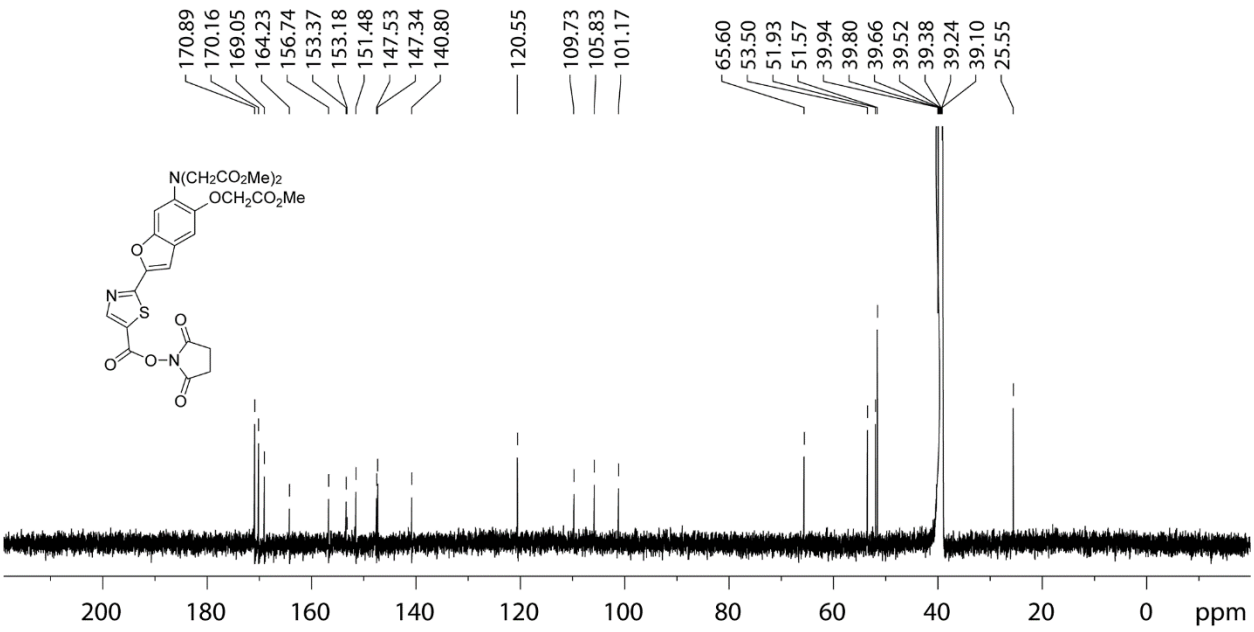

Figure S32. ^{13}C{^{1}H} NMR spectrum of compound **5** in DMSO-d_6.

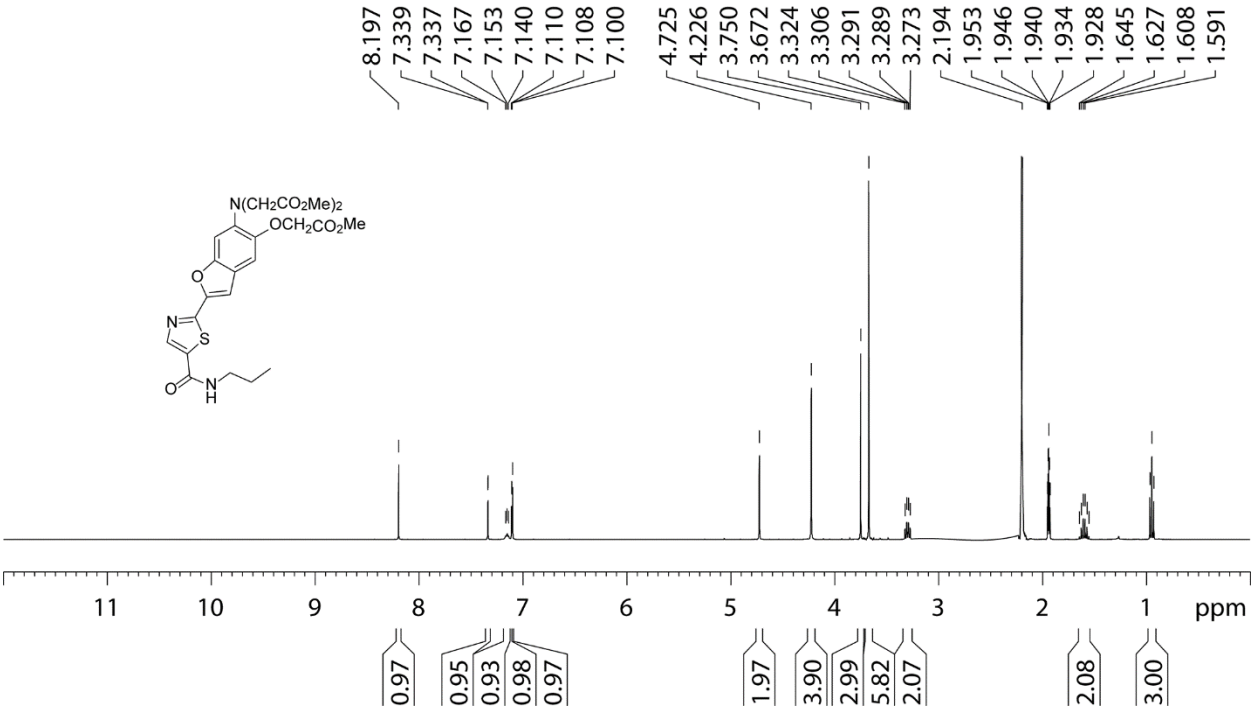

Figure S33. ^{1}H NMR spectrum of compound **6** in CD_3CN.

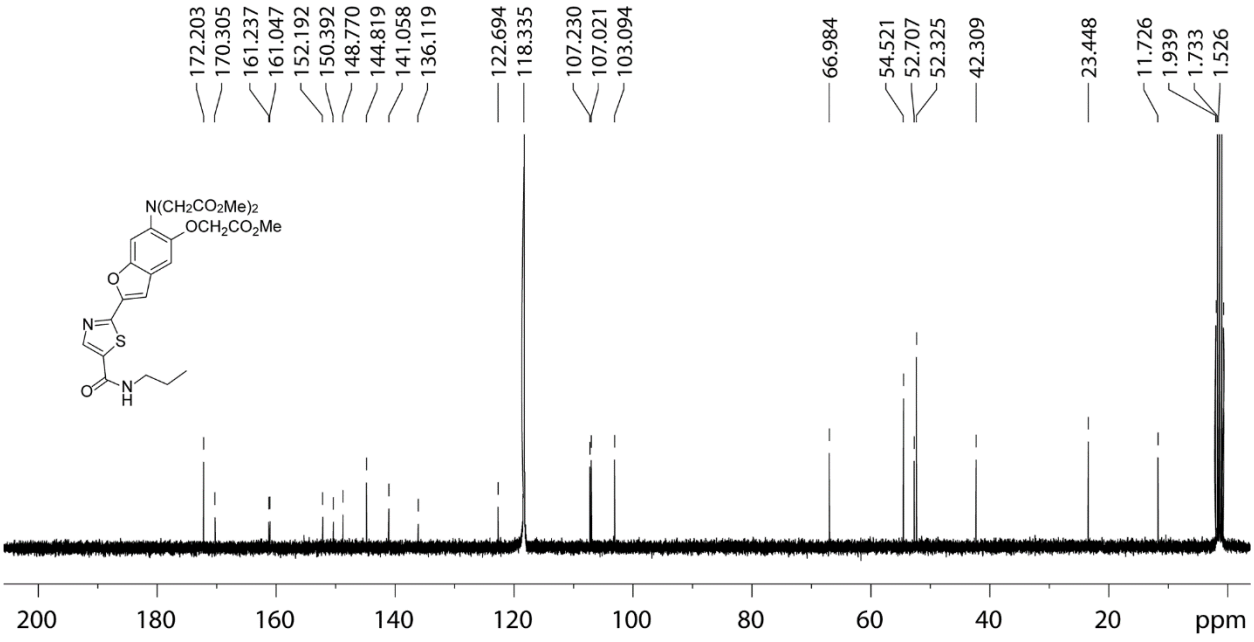

Figure S34. ^{13}C{^{1}H} NMR spectrum of compound **6** in CD_3CN.

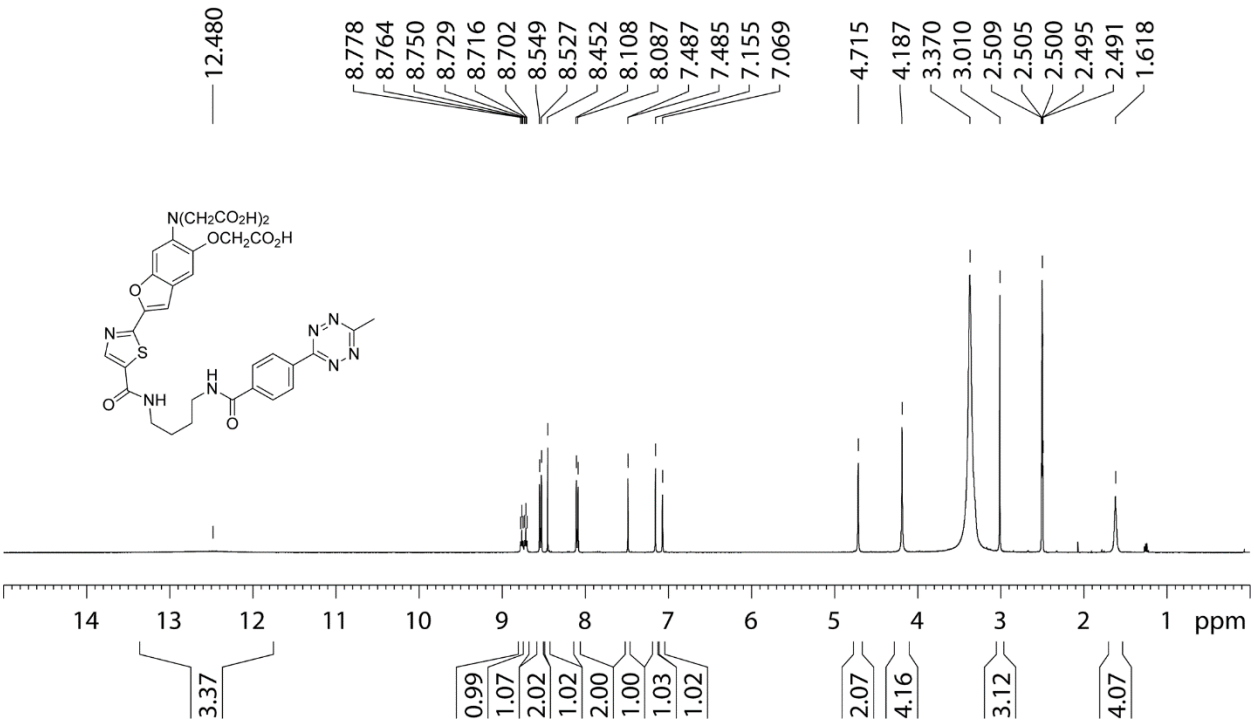

Figure S35. ^{1}H NMR spectrum of **Mag-*S*-Tz** in DMSO-d_6.

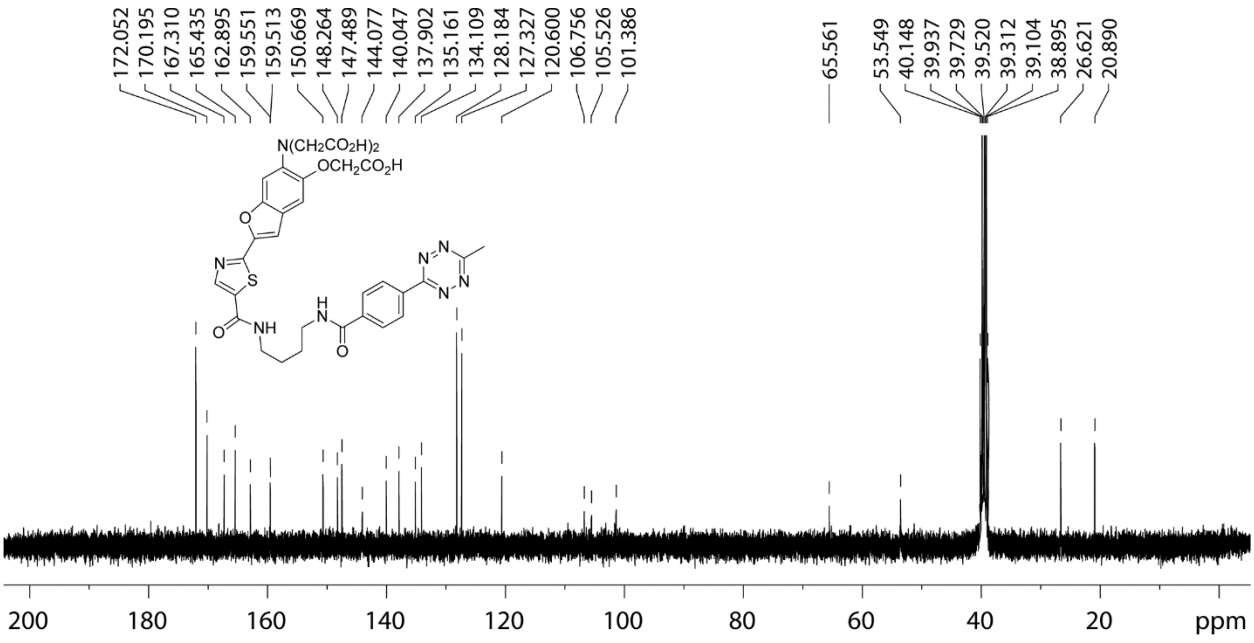

Figure S36. ^{13}C{^{1}H} NMR spectrum of **Mag-*S*-Tz** in DMSO-d_6.

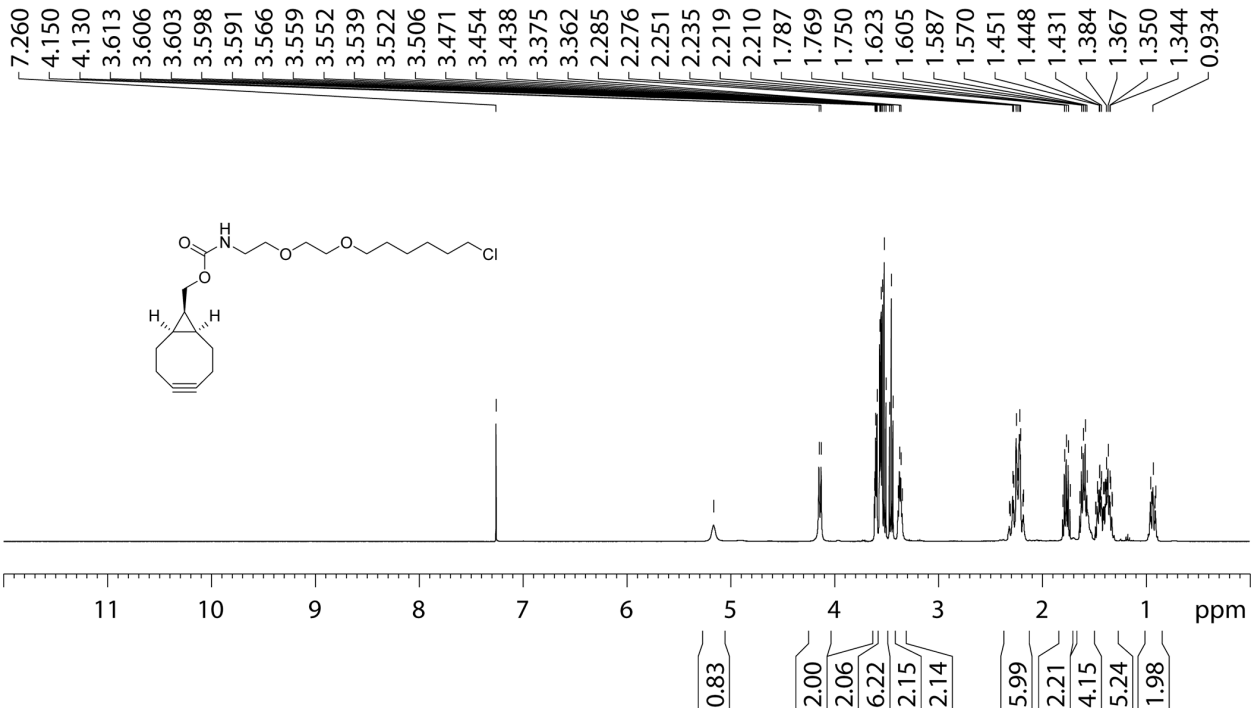

Figure S37. ^{1}H NMR spectrum of compound **BCN-Cl** in $CDCl_3$.

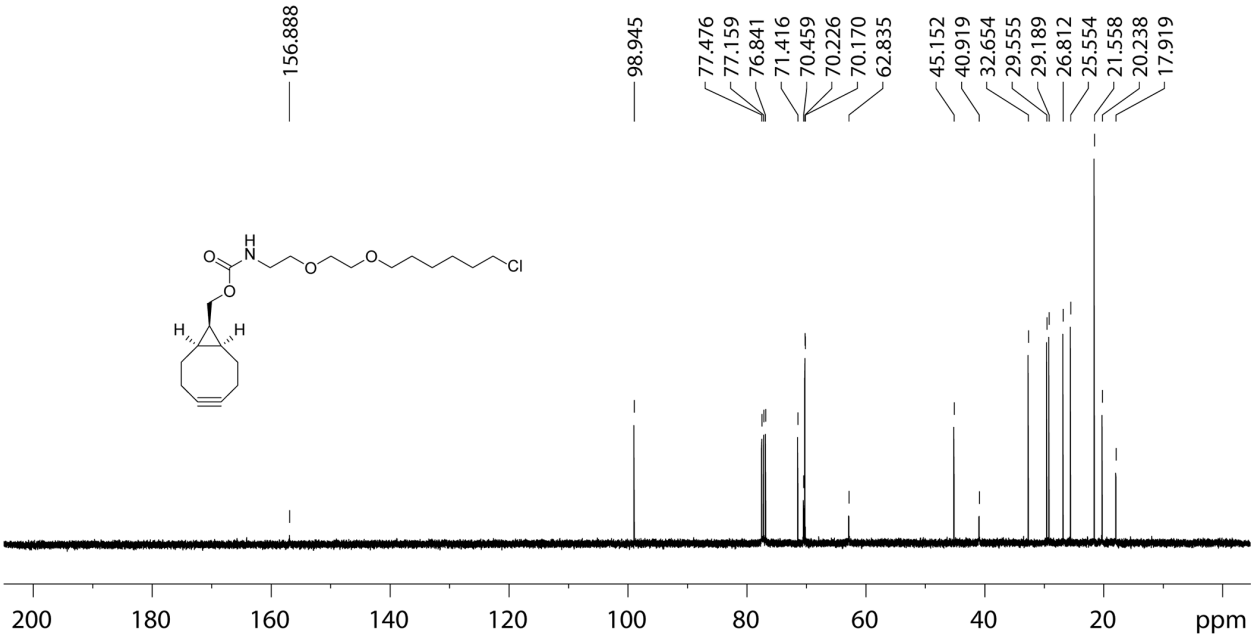

Figure S38. $^{13}C\{^{1}H\}$ NMR spectrum of compound **BCN-Cl** in $CDCl_3$.

S7. HPLC data for sensors

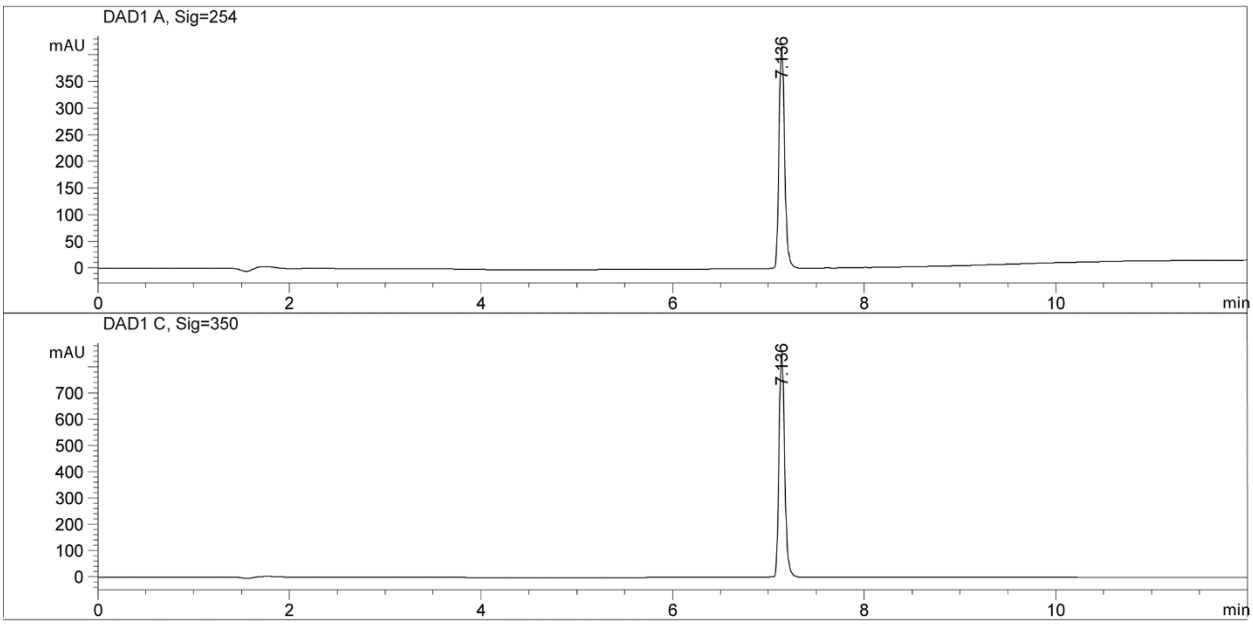

Figure S39. Reversed phase HPLC chromatogram of compound **6**, eluted with an acetonitrile/water (+0.1% TFA) gradient.

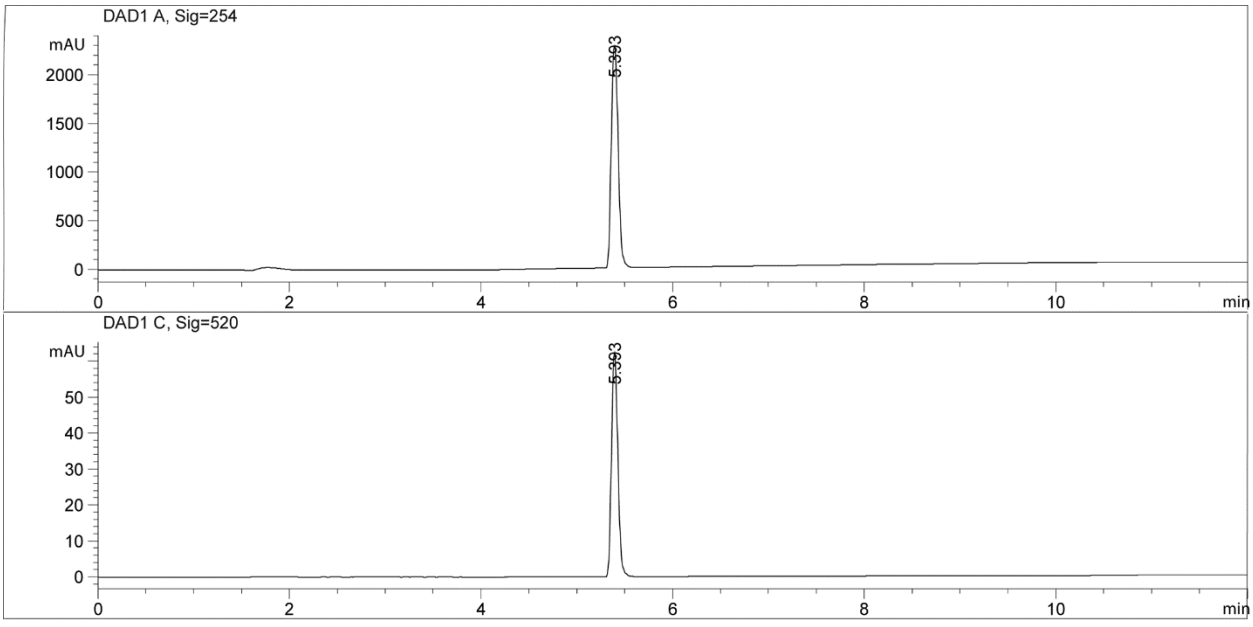

Figure S40. Reversed phase HPLC chromatogram of compound **7**, eluted with an acetonitrile/water (+0.1% TFA) gradient.

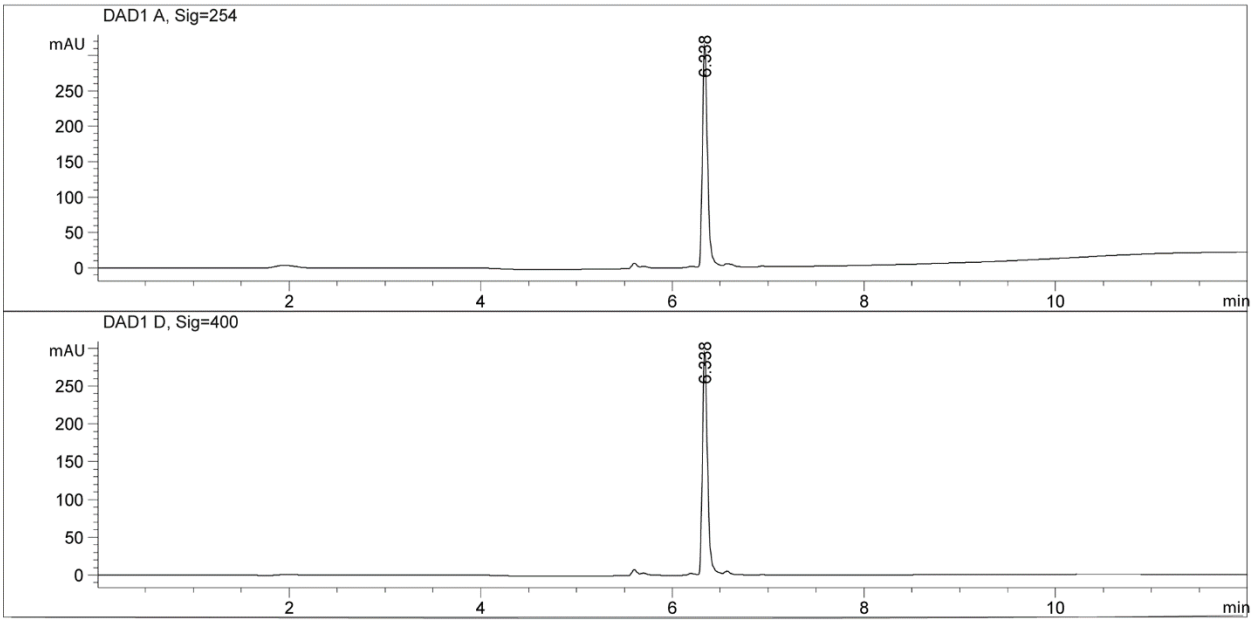

Figure S41. Reversed phase HPLC chromatogram of **Mag-*S*-Tz**, eluted with an acetonitrile/water (+0.1% TFA) gradient.

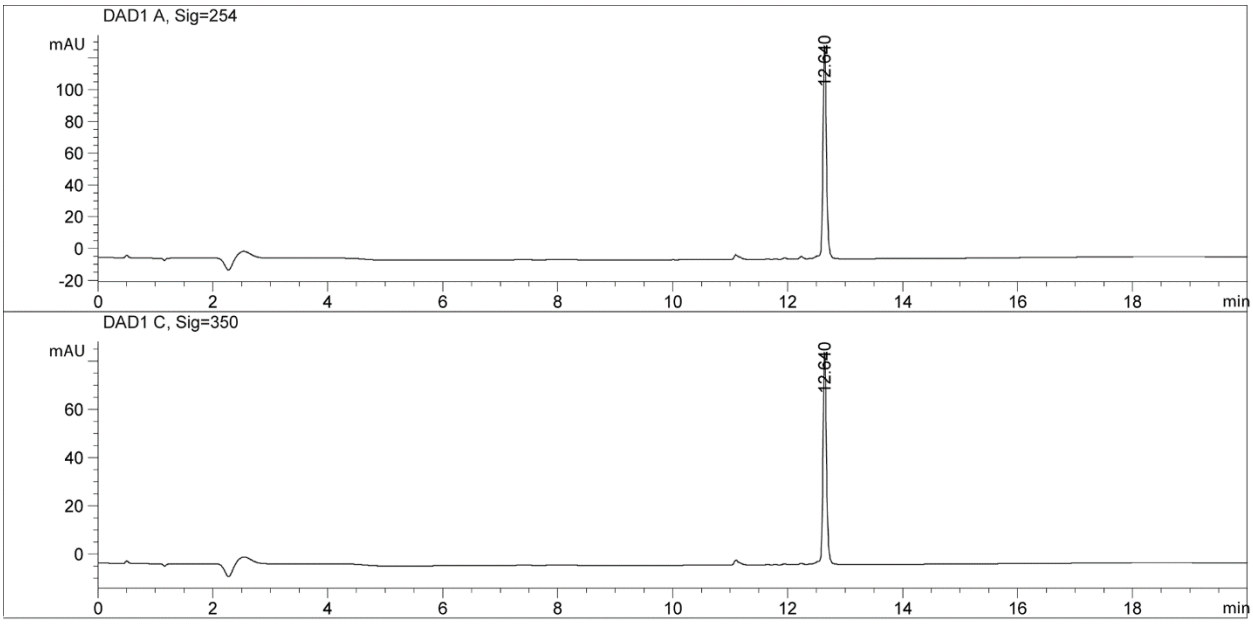

Figure S42. Reversed phase HPLC chromatogram of **Mag-*S*-Tz-AM**, eluted with an acetonitrile/water gradient.

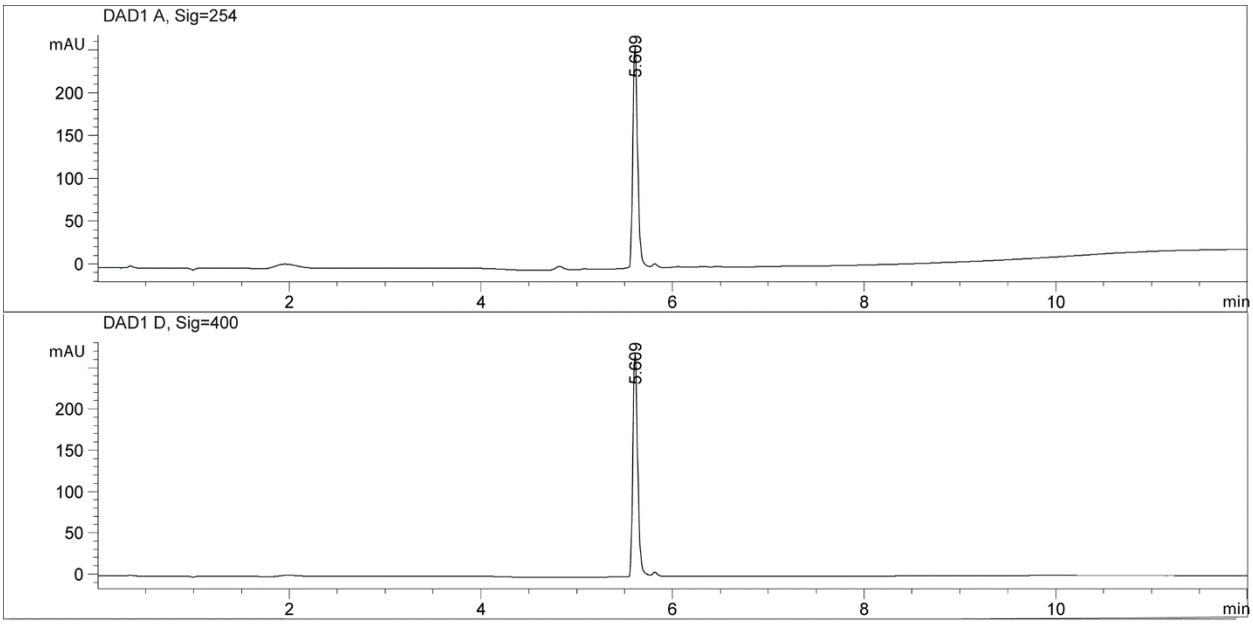

Figure S43. Reversed phase HPLC chromatogram of **Mag-*S*-Tz** activated with BCN. Sample eluted with an acetonitrile/water (+0.1% TFA) gradient.

S8. References

(1) Mashraqui, S. H.; Keehn, P. M. *J. Am. Chem. Soc.* **1982**, *104*, 4461.
(2) Dommerholt, J.; Schmidt, S.; Temming, R.; Hendriks, L. J. A.; Rutjes, F. P. J. T.; van Hest, J. C. M.; Lefeber, D. J.; Friedl, P.; van Delft, F. L. *Angew. Chem., Int. Ed.* **2010**, *49*, 9422.
(3) Los, G. V.; Encell, L. P.; McDougall, M. G.; Hartzell, D. D.; Karassina, N.; Zimprich, C.; Wood, M. G.; Learish, R.; Ohana, R. F.; Urh, M.; Simpson, D.; Mendez, J.; Zimmerman, K.; Otto, P.; Vidugiris, G.; Zhu, J.; Darzins, A.; Klaubert, D. H.; Bulleit, R. F.; Wood, K. V. *ACS Chem. Biol.* **2008**, *3*, 373.
(4) Grynkiewicz, G.; Poenie, M.; Tsien, R. Y. *J. Biol. Chem.* **1985**, *260*, 3440.
(5) Hargrove, A. E.; Zhong, Z.; Sessler, J. L.; Anslyn, E. V. *New J. Chem.* **2010**, *34*, 348.
(6) Martell, A. E.; Smith, R. M. *Critical stability constants*; Springer, 1974; Vol. 1.
(7) Goedhart, J.; von Stetten, D.; Noirclerc-Savoye, M.; Lelimousin, M.; Joosen, L.; Hink, M. A.; van Weeren, L.; Gadella, T. W. J.; Royant, A. *Nat. Commun.* **2012**, *3*, 751.